Ambient-Visible-Light-Mediated Enhanced Degradation of UV Stabilizer Bis(4-hydroxyphenyl)methanone by Nanosheet-Assembled Cobalt Titanium Oxide: A Comparative and DFT-Assisted Investigation

Po-Hsin Mao [1,†], Ta Cong Khiem [1,†], Eilhann Kwon [2], Hou-Chien Chang [3], Ha Manh Bui [4], Xiaoguang Duan [5], Hongta Yang [3,*], Suresh Ghotekar [6], Wei-Hsin Chen [7,8,9], Yu-Chih Tsai [1] and Kun-Yi Andrew Lin [1,*]

[1] Department of Environmental Engineering & Innovation and Development Center of Sustainable Agriculture, National Chung Hsing University, 250 Kuo-Kuang Road, Taichung 40227, Taiwan
[2] Department of Earth Resources and Environmental Engineering, Hanyang University, Seongdong-gu, Seoul 04763, Korea
[3] Department of Chemical Engineering, National Chung Hsing University, 250 Kuo-Kuang Road, Taichung 40227, Taiwan
[4] Department of Environmental Sciences, Saigon University, Ho Chi Minh 700000, Vietnam
[5] School of Chemical Engineering and Advanced Materials, The University of Adelaide, Adelaide, SA 5005, Australia
[6] Department of Chemistry, Smt. Devkiba Mohansinhji Chauhan College of Commerce and Science, University of Mumbai, Silvassa 396230, Dadra & Nagar Haveli (UT), India
[7] Department of Aeronautics and Astronautics, National Cheng Kung University, Tainan 701, Taiwan
[8] Research Center for Smart Sustainable Circular Economy, Tunghai University, Taichung 407, Taiwan
[9] Department of Mechanical Engineering, National Chin-Yi University of Technology, Taichung 411, Taiwan
* Correspondence: hyang@nchu.edu.tw (H.Y.); linky@nchu.edu.tw (K.-Y.A.L.)
† These authors contributed equally to this work.

Abstract: Bis(4-hydroxyphenyl)methanone (BHPM), a common ultraviolet stabilizer and filter (USF), is extensively added in sunscreens; however, BHPM is proven as an endocrine disruptor, posing a serious threat to aquatic ecology, and BHPM should be then removed. As sulfate radical ($SO_4^{\bullet-}$) could be useful for eliminating emerging contaminants, oxone appears as a favorable source reagent of $SO_4^{\bullet-}$ for degrading BHPM. Even though cobalt is a useful catalyst for activating oxone to generate $SO_4^{\bullet-}$, it would be even more promising to utilize ambient-visible-light irradiation to enhance oxone activation using cobaltic catalysts. Therefore, in contrast to the conventional cobalt oxide, cobalt titanium oxide (CTO) was investigated for chemical and photocatalytic activation of oxone to eliminate BHPM from water. Especially, a special morphology of nanosheet-assembled configuration of CTO was designed to maximize active surfaces and sites of CTO. Thus, CTO outperforms Co_3O_4 and TiO_2 in degrading BHPM via oxone activation. Furthermore, the substituent of Ti enabled CTO to enhance absorption of visible light and possessed a much smaller E_g. These photocatalytic properties intensified CTO's activity for oxone activation. CTO possessed a significantly smaller E_a of degradation of USFs than other catalytic systems. Mechanistic insight for degrading BHPM by CTO + oxone was explicated for identifying contribution of reactive oxygen species to BHPM degradation. The BHPM degradation pathway was also investigated and unveiled in details via the DFT calculation. These results validated that CTO is a superior cobaltic alternative for activating oxone to eliminate BHPM.

Keywords: UV filters; oxone; photocatalysis; titanium; cobalt; visible light

1. Introduction

For reducing harmful exposure to sunlight irradiation, sunscreens, containing ultraviolet stabilizers and filters (USFs), have become essential personal healthcare products.

Nevertheless, the extensive consumption of sunscreens has led to continuous discharge of USFs into various water bodies [1]. Unfortunately, many of these USFs have been proven as emerging contaminants because of their endocrine-disrupting effects and even carcinogenicity [2].

Amidst numerous USFs, benzophenones are the largest category and widely added in sunscreens [3]. Specifically, a particular benzophenone, bis(4-hydroxyphenyl)methanone (BHPM), appears as one of the most common benzophenones because BHPM is intensively adopted not only in cosmetics but also several products, including plastics, films, and fibers, for protecting these products from damage of light irradiation [3]. However, BHPM has been validated as an environmental hormone due to its endocrine-disrupting effect [4]. For preventing its negative impact on the water environment and even on public health, it would be necessary to eliminate BHPM from water.

As chemical oxidation technology is validated as an useful approach for removing toxic pollutants [5], sulfate radical ($SO_4^{\bullet-}$)-involved chemical oxidation technologies are appealing for eliminating emerging contaminants owing to the higher oxidation powder and longer half-life of sulfate radicals [6–8]. For generating $SO_4^{\bullet-}$, the commercial reagent, industrially available oxone has become favorable. Nonetheless, spontaneous generation of $SO_4^{\bullet-}$ from oxone would be extremely slow and inefficient; thus, oxone would require "activation" for expediting production of $SO_4^{\bullet-}$ to eliminate contaminants. To date, activation of oxone can be implemented by numerous approaches; nevertheless, applying metallic catalysts for accelerating oxone activation is recognized as the most factual means [9,10]. Amid various metallic materials, cobalt is the most potent metal in oxone activation [11], and conventionally, Co ions would be adopted as homogeneous catalysts for activating oxone. Unfortunately, addition of Co ions to solutions usually ends up causing serious concerns, namely extremely challenging collection of homogeneous metal ions as well as subsequent metal contamination. Therefore, tricobalt tetraoxide (Co_3O_4) has been employed as an alternative to Co ions for oxone activation [12], and the Co_3O_4 nanoparticle (NP) had been developed as a heterogeneous catalyst to activate oxone [13]. Nevertheless, Co_3O_4 NPs tend to agglomerate severely even in aqueous solutions and then possess much fewer active surfaces and sites for activating oxone [14,15].

As catalytic behaviors of heterogeneous catalysts would be correlated to morphologies, textural characteristics, as well as other properties, Co_3O_4 can be fabricated to enhance its catalytic activities through designing Co_3O_4 with advantageous morphologies and physiochemical properties [7,12,16]. Thus, it would be promising to fabricate Co_3O_4 into superior nanostructures, which would provide large contact surfaces and active sites. On the other hand, while Co_3O_4 would be a suitable activator for oxone, recently, facilitating oxone activation via photocatalysis, especially by ambient visible light, can be a readily accessible strategy for enhancing degradation of contaminants [17,18]. Therefore, it would be even more useful to develop a Co-based catalyst with an advantageous nanostructure and ambient-visible-light-driven photocatalytic activity. To this end, a Ti-substituted analogue to Co_3O_4, cobalt titanium oxide (Co_2TiO_4) (CTO), is particularly developed here, as CTO is still comprised of Co species, but the substituent of Ti in CTO enhances photocatalytic activities of CTO, making it a dual-functional heterogeneous Co-based catalyst [19,20]. Specifically, a unique nanostructure of CTO would be configured here to afford a CTO consisting of nanosheets (NSs), which would be assembled and interpenetrated to produce an NS-assembled nanocluster. Such a CTO would be an auspicious activator for oxone under ambient visible light to enhance eliminating organic contaminants from water [21–24]. As very few studies have ever looked into visible-light-mediated activation of oxone by CTO for degradation of USFs, the present study can for the first time offer valuable insights for further realizing the catalytic and photo-catalytic behaviors of CTO in comparison to conventional Co_3O_4 and TiO_2 NPs. The detailed degradation mechanism of BHPM by CTO are also discussed via experimental and theoretical investigations.

2. Experimental

In this study, reagents and materials all were purchased and employed directly without purification. Preparation of NS-assembled CTO by a hydrothermal protocol is illustrated in Figure 1a. The details of preparation and characterization of materials, BHPM degradation by oxone, and computer-aided computation are described in the supplementary material.
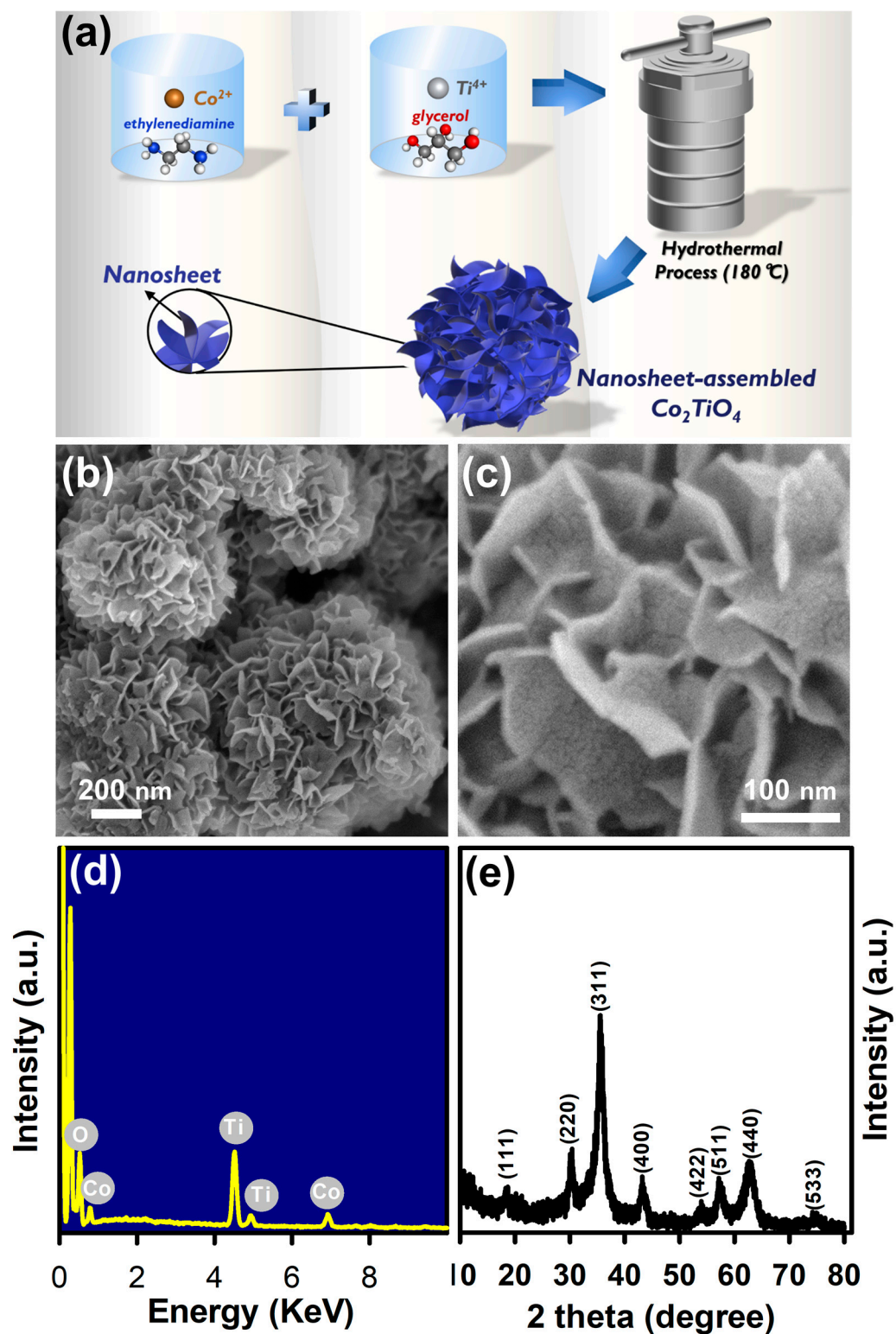
Figure 1. (**a**) Scheme of fabrication of CTO. Morphologies of CTO: (**b**,**c**) SEM images, (**d**) EDS, and (**e**) XRD pattern.

3. Results and Discussions

3.1. Physical and Chemical Properties of CTO

At first, the appearance of CTO is displayed in Figure 1b, in which several granules can be observed. Visibly, these granules were sub-micrometer-sized and comprised of irregularly curved sheets. The detailed image in Figure 1c then demonstrates that those sheets were very thin, with a thickness of ~10 nm, and these NSs were interpenetrated and assembled to afford a granule. Figure 1d shows the chemical composition of the NS-assembly, and Co, Ti, and O elements could be detected without other elements. More importantly, its crystalline structure was obtained (Figure 1e), and a series notable peaks were detected and indexed to Co_2TiO_4 (PDF#: 39-1410), confirming that this Co/Ti/O-containing material was Co_2TiO_4 (CTO). Figure 2 further reveals the elemental mapping analyses of NS-assembled CTO, and Co, Ti, and O elements can be evenly distributed over the scanned area of CTO. These results indicate that the NS-assembled CTO were successfully fabricated.

As a large amount of glycerol was employed here, glycerol would be converted to glycerate, which would coordinate with Co^{2+}/Ti^{4+} to form spherical granules [25]. On the other hand, since ethylenediamine (EDA) was also added during the preparation of CTO, EDA would temporarily coordinate with metal ions (e.g., Co^{2+} and Ti^{4+}) to influence the growth rate of Co^{2+}/Ti^{4+}-glycerate coordination [26]. Thus, the addition of EDA would usually enable the formation of sheet-like structures, which might be further self-assembled to afford flower-like clusters as CTO prepared in this study [26].

For comparisons, the commercial TiO_2 and Co_3O_4 NPs were also employed here. Figure S1 displays the morphology of Co_3O_4 NP, which were in sizes of a few tens of nanometers, and its crystalline structure (Figure S1b) was well-indexed to Co_3O_4 (PDF# 78-1970) [27–30]. On the other hand, the commercial TiO_2 NP (i.e., P25 TiO_2) is shown in Figure S2a, exhibiting sizes of a few tens of nanometers, and its corresponding XRD result could be properly in line with the reported result of P25 TiO_2 comprised of rutile (R) and anatase (A) phases.

As CTO exhibited an interesting and distinct morphology compared to conventional spherical NPs, its textural properties were then examined and further compared with Co_3O_4 and TiO_2 NPs. Figure 3a reveals a gas adsorption isotherm of CTO that led to a significant amount of N_2 adsorption with a notable hysteresis loop, as the sheet-like nanostructures would enable CTO to exhibit a large surface; thus, CTO can show a substantially high surface area of 232 m^2/g. Its distribution of porosity shown in Figure 3b further validates that NS-assembled CTO exhibited mesoscale pores in the range of 2~60 nanometers, and the porosity of CTO was 0.50 cc/g. Moreover, a closer view of the sheet of CTO (Figure 1c) actually unveiled some fissures on these sheets; these fissures would further provide very small pores as observed in the pore size distribution (Figure 3a) to increase surface areas. The gas adsorption isotherms of Co_3O_4 as well as TiO_2 NPs were also measured and included in Figure 3a. Nevertheless, N_2 adsorption to TiO_2 was noticeably lower than that to CTO, whereas N_2 sorption to Co_3O_4 was even much lower, probably attributed to serious aggregation of NPs. Therefore, the surface areas of TiO_2 and Co_3O_4 were 42 and 2 m^2/g, respectively. Furthermore, the pore volumes of TiO_2 and Co_3O_4 were also much smaller as 0.47 and 0.01 cc/g. These results indicate that CTO revealed much more advantageous textural properties than Co_3O_4 and TiO_2 owing to its NS-assembled configuration.
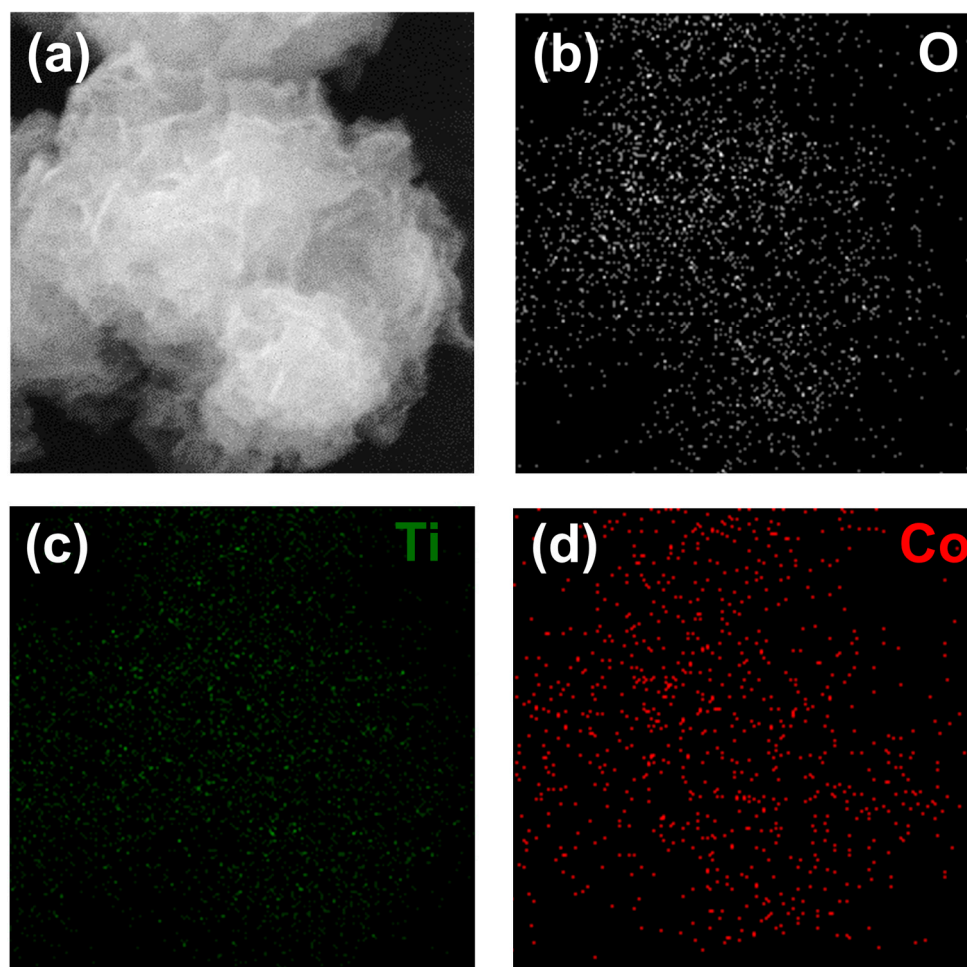
**Figure 2.** (**a**) Scanned region of CTO; (**b**–**d**) elemental mapping analyses of CTO.

Moreover, the diffuse reflectance spectra (DRS) of these catalysts were then obtained in Figure 3c. In the cases of pristine TiO_2 and Co_3O_4 without modifications, the pristine TiO_2 showed a narrow absorption range from 200 to 400 nm, whereas the pristine Co_3O_4 NP revealed a wide and broad absorption range from 200 to 800 nm [31]. On the other hand, CTO also exhibited a broad absorption range from 200 to 800, indicating that CTO can adsorb irradiation of the visible-light range. Correspondingly, their Tauc plots are displayed in Figure 3d–f for further determining their energy band gaps (E_g). E_g of TiO_2 was calculated as 3.20 eV, which was consistent to the reported value of P25 TiO_2 [32–34], whereas E_g of Co_3O_4 was estimated as 1.76 eV, which was in line with E_g reported in literatures [31]. E_g of CTO was then determined as 1.60 eV, which would be slightly lower than the pristine Co_3O_4 and TiO_2, demonstrating that CTO would be a favorable photocatalyst [35].

Furthermore, as electrochemical property plays an important role in oxone activation, electrochemical characteristics of these catalysts were then characterized to determine their redox potentials, electron transports, and possible active areas. At first, cyclic voltammetry (CV) curves of CTO, TiO_2, and Co_3O_4 in a potential window of $-0.2\sim0.6$ V using 1 M KOH are displayed in Figure 4a. Noticeably, CTO exhibited a significantly higher current area than Co_3O_4 and TiO_2, demonstrating that CTO possessed a higher interfacial reaction rate. This would be because CTO had the much larger surface and pores, which then serve as ion reservoirs, minimizing the diffusion distance to the inner surface and expediting the diffusion process of ions in the electrode. Thus, CTO could exhibit much more advantageous electrochemical characteristics [36]. Moreover, the CV curves of CTO at multiple scanning rates are shown in Figure 4b. When the scanning rate became higher, peak currents of

oxidation and reduction increased due to the change in the diffusion layer thickness. The results of the linear sweep voltammogram (LSV) are then revealed in Figure 4c, in which CTO also showed a much smaller overpotential (at 1.0 mA), validating that CTO exhibited more advantageous electron transport and mass transfer efficiency than TiO_2 and Co_3O_4. Additionally, the Nyquist plots of these catalysts were then obtained to examine the charge transfer abilities of these catalysts (Figure 4d), and CTO exhibited the smaller diameter of the semi-circle at a higher-frequency region, which represented a lower charge-transfer resistance, indicating that CTO had a much faster electron transfer rate [37].
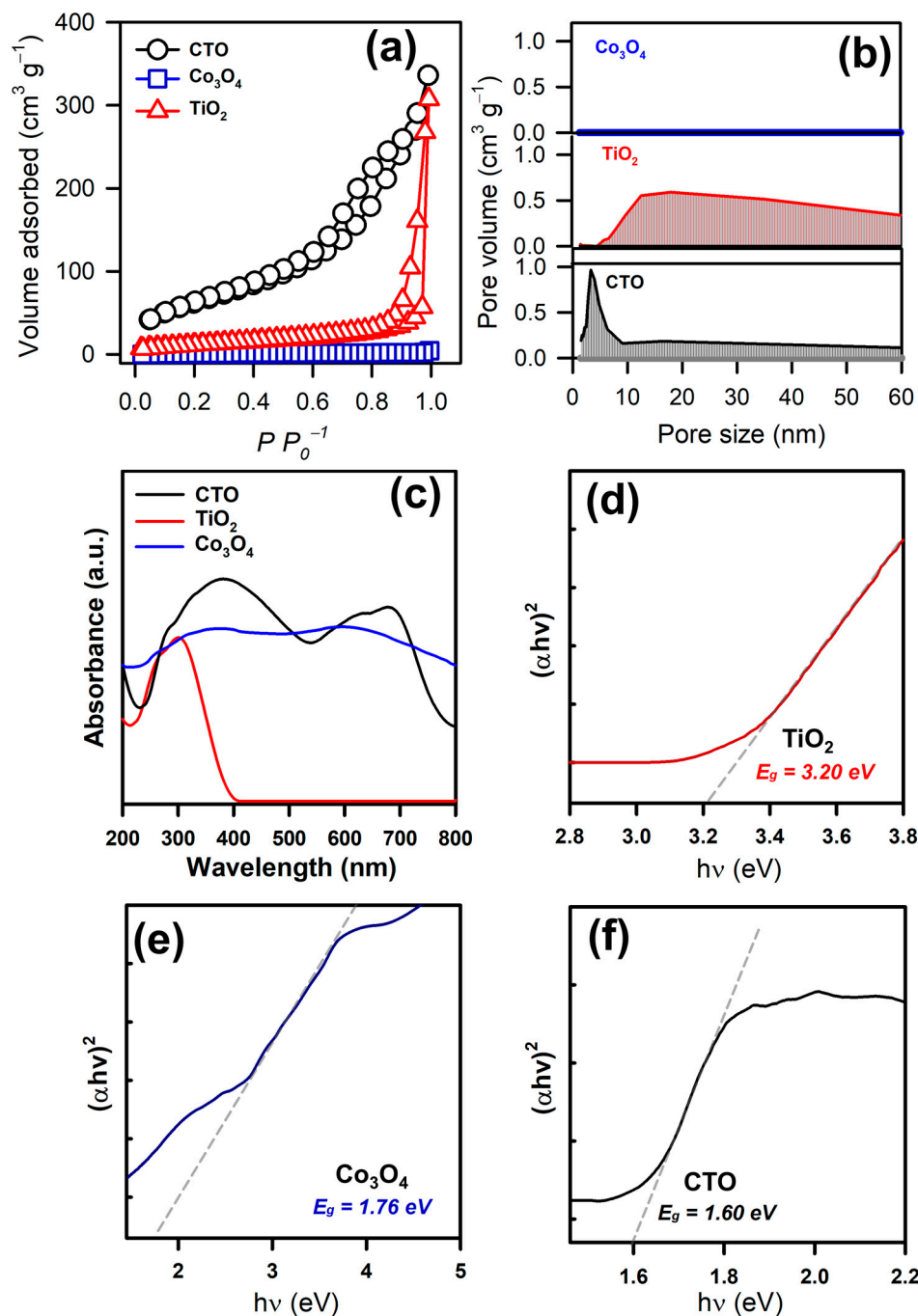
Figure 3. (**a**) N_2 sorption isotherms, (**b**) pore size distributions, (**c**) DRS, and (**d–f**) Tauc plots of CTO, TiO_2, and Co_3O_4.
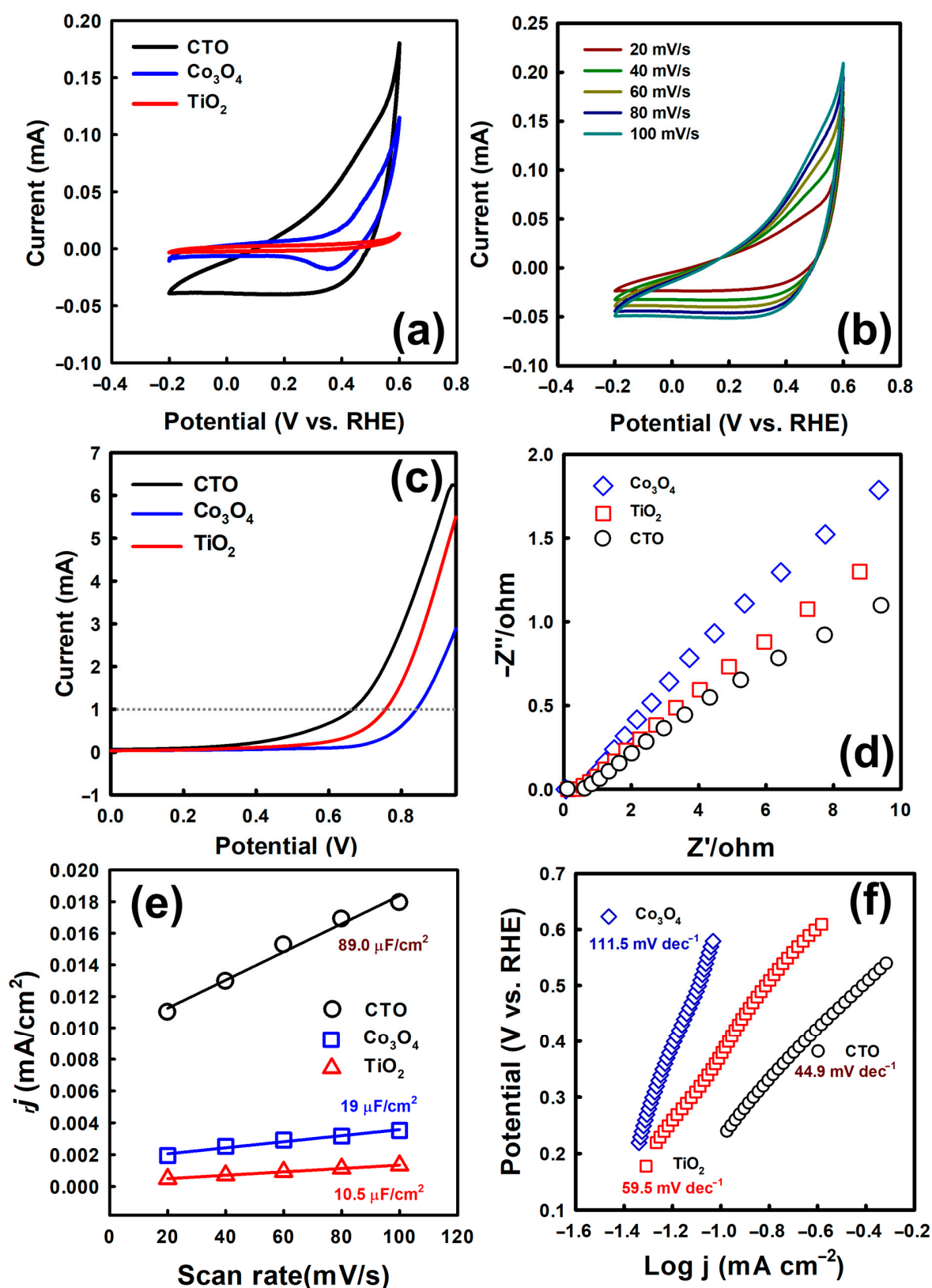
Figure 4. (**a**) CV curves of different catalysts at a scan rate of 60 mV/s, (**b**) CV curves of CTO at different scan rates, (**c**) LSV curves of different catalysts at a scan rate of 1 V/s, and (**d**) EIS Nyquist plots of different catalysts. A 1 M KOH was used as the electrolyte; (**e**) ECSA curves and (**f**) Tafel plots of CTO, TiO$_2$, and Co$_3$O$_4$.

For examining the active sites of these catalysts, the double-layer capacitance (C_{DL}) would be then investigated with an electrolyte containing 200 mg/L oxone and 0.5 M Na_2SO_4 to further determine the electrochemical surface area (ECSA). The scan rate-dependent CV curves of CTO, TiO_2, and Co_3O_4 in the non-Faradaic region are displayed in Figure S3a–c. The C_{DL} value was then calculated by $C_{DL} = J_m/v$, where J_m denotes current density, and v indicates the scanning rate. J_m would be obtained by averaging values between anodic and cathodic current densities with the central potential based on $J_m = (|J_a| + |J_c|)/2$. Through regressing J_m with v, slopes of the fitted curves (C_{DL}) of these catalysts are expressed in Figure 4e. CTO exhibited a significantly higher C_{DL} value (89 μF/cm^2) than Co_3O_4 and TiO_2, validating that CTO had more active site areas. These characterizations demonstrate that this NS-assembled CTO exhibited much superior physiochemical properties than the pristine Co_3O_4, and TiO_2, making it a promising oxone activator to degrade BHPM. Moreover, the electro-catalytic behaviors of these catalysts were then examined by Tafel analyses, and their Tafel slopes are displayed in Figure 4f, in which CTO exhibited a considerably smaller slope of 44.9 mV dec^{-1} than the Tafel slopes of Co_3O_4 (i.e., 111.5 mV) and TiO_2 (59.5 mV). This suggests that CTO possessed a much more superior electron transfer kinetics than the commercial Co_3O_4 and TiO_2.

3.2. Degradation of BHPM and Decomposition of Oxone by CTO

Firstly, it would be imperative to test whether BHPM might be removed by CTO due to adsorption and photocatalytic decomposition. Figure 5a shows that when CTO alone existed in an BHPM solution under ambient-visible-light irradiation, BHPM concentration was slightly decreased to $C_t/C_0 = 0.87$, suggesting that CTO itself was not efficient for eliminating BHPM within 20 min either through adsorption or photocatalysis. In the case of oxone present under light irradiation, BHPM was barely degraded within 20 min, demonstrating that auto-dissociation of oxone could not effectively eliminate BHPM. Next, when CTO and oxone were simultaneously added under light irradiation, BHPM was expeditiously eliminated and completely removed in 10 min. Thus, CTO seemed to activate oxone for producing reactive oxygen species (ROS) to quickly eliminate BHPM. Further, when the light irradiation was off, BHPM could be still quickly eliminated, and C_t/C_0 could also approach zero within 20 min. These results demonstrate that CTO itself could already activate oxone to degrade BHPM, and the light irradiation might enable CTO to exert additional photocatalytic activities for BHPM degradation.

For comparisons, the commercial Co_3O_4 and TiO_2 NPs were also examined for their activities of activating oxone. Figure 5a displays that TiO_2 NP almost could not cause degradation of BHPM, as the light irradiation was in the visible range instead of ultraviolet range. Co_3O_4 NP, on the other hand, could slightly cause decomposition of BHPM, and the corresponding C_t/C_0 approached 0.66 within 20 min. These results both indicated that the pristine commercial TiO_2 and Co_3O_4 NPs under the light irradiation were incapable of activating oxone to degrade BHPM efficiently. For further distinguishing catalytic activities of these catalysts for degradation of BHPM, the pseudo-first-order equation: $C_t = C_0 \cdot e^{-kt}$ was adopted, where k represents an observed rate constant. As the k for BHPM elimination by CTO under light irradiation would be 0.979 min^{-1} (Figure 5b), the k by CTO without light would be slightly lower (i.e., 0.340 min^{-1}), validating that light enhanced oxone activation and BHPM elimination. Moreover, the corresponding k for Co_3O_4 NP and TiO_2 NP under light irradiation were significantly smaller as 0.021, and 0.007 min^{-1}, respectively, confirming that both the pristine Co_3O_4 and TiO_2 exhibited much lower catalytic activities than CTO for oxone activation.
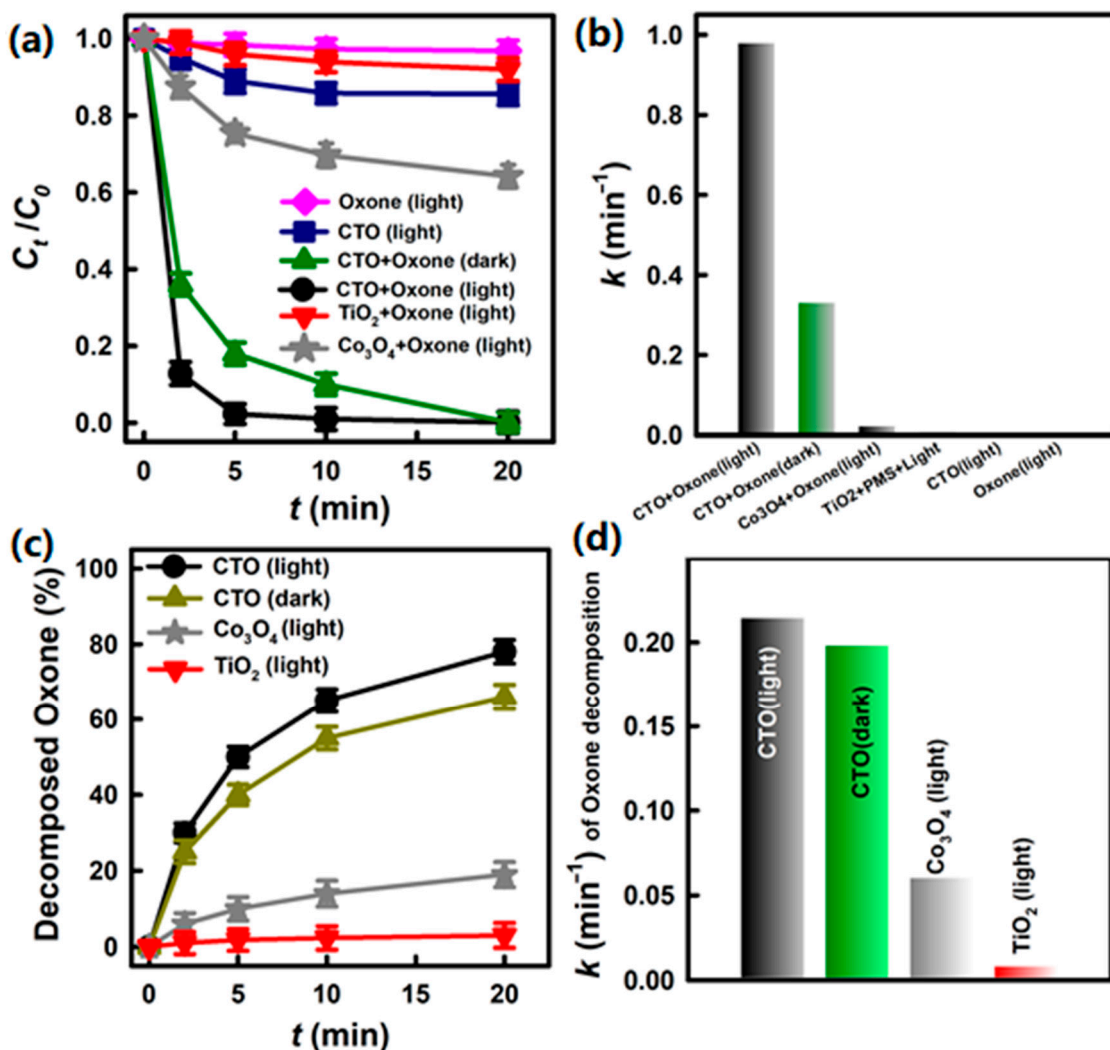
Figure 5. (**a**) Comparison of BHPM degradation by oxone alone, adsorption to catalysts, and oxone activated by CTO, TiO$_2$, and Co$_3$O$_4$; (**b**) rate constant of BHPM degradation using oxone activated by catalysts (catalyst = 200 mg/L, oxone = 200 mg/L, T = 300 K); (**c**) decomposition of oxone by different catalysts; and (**d**) rate constants of oxone decomposition by catalysts.

Moreover, it would be interesting to further explore the dissociation of oxone induced by these catalysts. Figure 5c shows oxone dissociation by catalysts as a function of time, and CTO would quickly cause dissociation of oxone either under light irradiation or not; nevertheless, the light irradiation certainly enhanced the dissociation of oxone with a higher rate constant, as shown in Figure 5d. This suggests that the light irradiation might contribute to photocatalytic activation of oxone by CTO. On the other hand, oxone dissociation by the pristine Co$_3$O$_4$ and TiO$_2$ NPs were significantly slower, validating that these pristine NPs were much less efficient than CTO. These results all indicate that CTO exhibited much higher catalytic activities for oxone activation than Co$_3$O$_4$, and TiO$_2$, possibly because of more superior electrochemical and photocatalytic properties of CTO.

Generally, oxone activation by cobalt-based catalysts would be associated with contribution of Co species through the following reactions [38]:

$$Co^{II}@catalyst + HSO_5^- \rightarrow Co^{III}@catalyst + SO_4^{\bullet-} + OH^- \tag{1}$$

$$Co^{III}@catalyst + HSO_5^- \rightarrow Co^{II}@catalyst + SO_5^{\bullet-} + OH^- \tag{2}$$

$$SO_5^{\bullet-} \rightarrow SO_4^{\bullet-} + \frac{1}{2}O_2 \tag{3}$$

Hence, it was interesting to further analyze surface chemistry of CTO. Figure 6a first unveils the Co2p curve of CTO, and it could be then analyzed to reveal a series of notable peaks at 778.2, 780.6, 795.4, and 796.8 eV. These peaks at 778.2 as well as 795.4 eV were related to Co^{3+} of $Co2p_{3/2}$ and $Co2p_{1/2}$, while the peaks at 780.6 and 796.8 were both Co^{2+} of Co_3O_4. On the other hand, the Ti2p spectrum of CTO (Figure 6b) was also obtained, and it was analyzed to reveal distinct peaks at 457.5 as well as 463.3 eV, and the difference between these two peaks, i.e., 5.8 eV, indicated that those peaks would correspond to Ti^{3+}, which was consistent to the reported species [39]. Furthermore, the O1s spectrum of CTO was then also analyzed (Figure 6c), and two peaks can be afforded at 529.4 and 530.8 eV, corresponding to the lattice oxygen (O_L) and the chemisorbed oxygen (O_C).
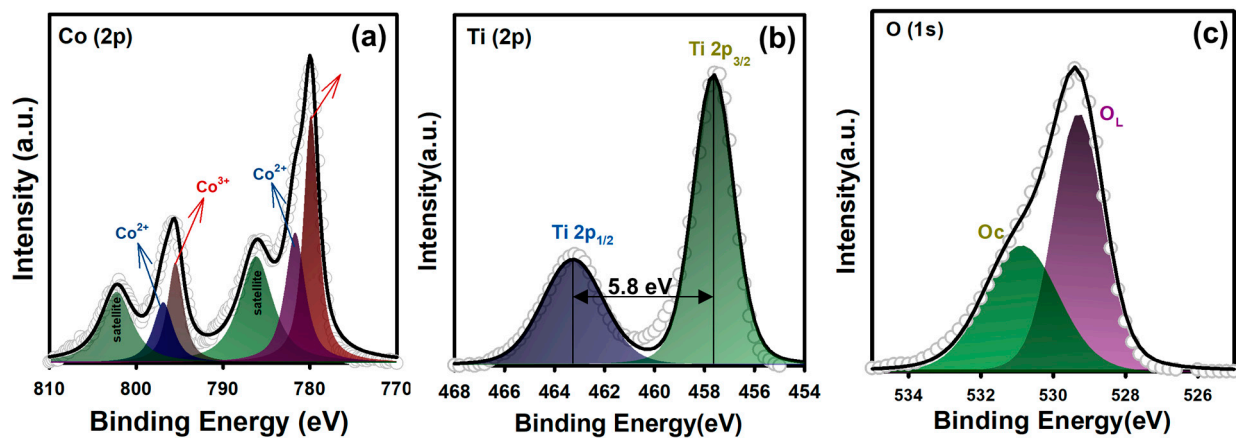

Figure 6. XPS analyses: (**a**) Co2p, (**b**) Ti2p, and (**c**) O1s of CTO.

These analyses suggested that activating oxone using CTO was partially ascribed to these Co species (Co^{3+} and Co^{2+}) for decomposing oxone to produce ROS (e.g., $SO_4^{\bullet-}$) even without light irradiation. Thus, Figure 5a displays that CTO without light irradiation also caused rapid BHPM elimination within 20 min. Nevertheless, since CTO could exhibit photocatalytic activities, oxone might be also activated by the CTO-induced photocatalytic process, in which photo-catalytically induced e^- as well as h^+ would be generated based on the following reactions [40]:

$$CTO + hv \rightarrow e^- + h^+ \tag{4}$$

These resulting e^-/h^+ would then encounter with oxone for producing ROS via the following reactions [41]:

$$HSO_5^- + e^- \rightarrow SO_4^{-\bullet} + HO^- \tag{5}$$

$$HSO_5^- + h^+ \rightarrow SO_5^{-\bullet} + H^+ \tag{6}$$
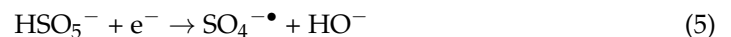
The high oxidation potentials of these ROS would then attack and cause decomposition of BHPM.

3.3. Influence of Catalysts/Oxone Dosages on BHPM Elimination

While CTO efficiently activated oxone to eliminate BHPM, it would be interesting to investigate how CTO and oxone dosage influenced BHPM elimination. Figure 7a reveals BHPM degradation efficiency, which was obviously enhanced by increasing CTO dosage. Specifically, at 100 mg/L of CTO, BHPM was gradually eliminated as C_t/C_0 reached zero in 20 min. The k would be calculated as 0.7425 min^{-1}. Once CTO is augmented to 200 mg/L, BHPM would be fully removed in a shorter time. Complete removal could be reached within a much briefer period (i.e., ~5 min) at 300 mg/L. k was 0.979 min^{-1} and then 1.411 min^{-1} at CTO = 200 and then 300 mg/L, indicating the merit of higher CTO concentration in BHPM elimination as a result of relatively abundant catalytic sites to expedite activation of oxone to produce ROS. A higher CTO dosage would lead to much

faster kinetics of BHPM degradation. Such a phenomenon has been also observed in several studies of using oxone to degrade contaminants because a higher dosage of catalyst would provide more reactive surface areas of catalysts, which would facilitate oxone activation and then enhance degradation [42–44].
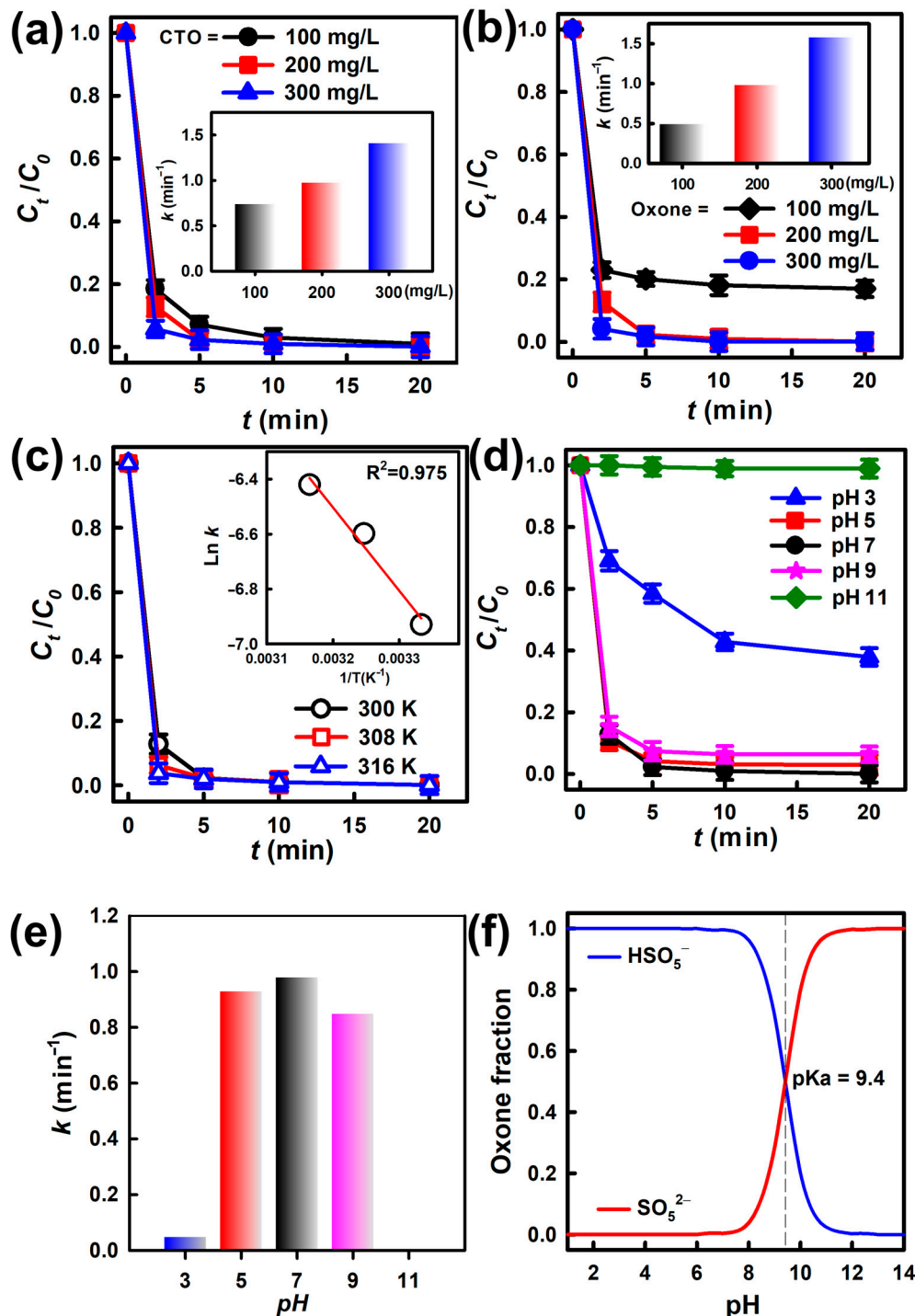
Figure 7. Degradation of BHPM by oxone by CTO + oxone: (**a**) effect of catalyst concentration, (**b**) effect of oxone concentration, (**c**) effect of temperature, and the corresponding plot of Ln k vs. 1/T; (**d**) effect of pH value and the corresponding (**e**) degradation kinetics and (**f**) species of oxone at various pH (catalyst = 200 mg/L; oxone = 200 mg/L; T = 300 K).

Furthermore, the effect of oxone dosage on BHPM elimination would be investigated would be examined (Figure 7b). When a relatively low amount of oxone (i.e., 100 mg/L)

was present, merely 80% of BHPM would be degraded in 20 min due to the insufficiency of radicals [43,44]. When oxone dosage was then increased to 200 mg/L, BHPM elimination was completed in 10 min. An even higher oxone at 300 mg/L would also cause even faster full elimination of BHPM (Figure 7b). In addition, the corresponding k with different oxone dosages were summarized in the inset. Its k at 100 mg/L of oxone would be estimated to be 0.490 min^{-1}. It would be considerably increased to 0.979 and 1.577 min^{-1} at oxone concentrations of 200 and 300 mg/L, respectively, thereby indicating the importance of sufficient oxone dosage for full removal of BHPM. Although a higher dosage of oxone would improve degradation, the degradation efficiency and kinetics would not be proportional to the dosage of oxone, as there would be a saturation for oxone present on the surface of catalysts [43,44]. Therefore, the improvement of degradation kinetics would be limited even though an even higher oxone dosage is employed [8,45,46].

3.4. Influences of Temperature and pH to BHPM Elimination

For further investigating catalytic behaviors of CTO, BHPM degradation was then implemented at various temperatures (300, 308, and 316 K) in Figure 7c. In general, the BHPM degradation was considerably accelerated at higher temperatures. Specifically, at 300 K, the full elimination of BHPM would be achieved quickly with a k of 0.979 min^{-1}. Since it was further elevated to 308 K and 316 K, BHPM degradation became much faster, as C_t/C_0 became zero in much shorter times, and the k values would be considerably increased to 1.360 min^{-1} (308 K) as well as 1.630 min^{-1} (316 K).

Further, since the k rose at higher temperatures, the correlation of k with T was then associated for obtaining E_a by the following equation:

$$Lnk - \ln A = -E_a/RT \tag{7}$$

The inset of Figure 7c shows the relationship between $Ln\ k$ and $1/T$, which was properly fitted linearly (R^2 > 0.95). Thus, the E_a of BHPM degradation would be 25.1 kJ/mol, which was smaller than most of the reported E_a of USF degradation by other processes in Table S1 [47–49], thereby confirming that CTO was certainly an advantageous and highly useful catalyst for degrading BHPM.

On the other hand, it was also critical to examine how pH would affect BHPM elimination. Figure 7d unveils that BHPM was fully eliminated rapidly under the neutral status with k of 0.979 min^{-1} (Figure 7e). As pH was adjusted to 5, BHPM elimination also proceeded very rapidly with a k of 0.930 min^{-1}; nevertheless, BHPM elimination was slightly affected (C_t/C_0 at 20 min = 0.026), and BHPM was not completely eliminated in 20 min. When the solution became pH = 3, C_t/C_0 was 0.4, and k decreased to 0.051 min^{-1}. BHPM elimination by CTO-activated oxone is thus less effective under the low-pH condition, probably because oxone becomes relatively inert under the low-pH condition [50], thus inhibiting oxone activation. Moreover, the resulting ROS (e.g., SO$_4$$^{•-}$, $^{•}$OH) would be rapidly depleted by H$^+$ according to the following equations, leading to the less efficient BHPM elimination:

$$H^+ + {}^{•}OH + e^- \rightarrow H_2O \tag{8}$$

$$H^+ + SO_4{}^{•-} + e^- \rightarrow HSO_4{}^- \tag{9}$$

In addition, as pKa of BHPM is 7.6 [51], BHPM might exhibit positive charges under acidic conditions. Thus, the less effective degradation of BHPM at pH 3 would be related to the more intensive revulsion between CTO and BHPM at low pH. Furthermore, H$^+$ might react with free radicals at low pH, thus suppressing BHPM elimination. Furthermore, hydrogen bonding of O-O and H$^+$ on oxone itself in acidic environments would limit reactions of oxone with CTO [52].

Furthermore, BHPM elimination was also influenced under alkaline conditions. Specifically, at pH = 9, BHPM elimination was marginally influenced, as C_t/C_0 was 0.06 at 20 min, and its k was 0.840 min^{-1}. Moreover, once pH changed to 11, a highly alkaline condition, BHPM was barely degraded in 20 min. This validates the negative impact of alkaline

environment on BHPM elimination, which would be possibly correlated to the much more intensive electrostatic repulsion between the relatively anionic surface of CTO and SO_5^{2-}, as pH exceeded the pKa of oxone = 9.4, as revealed in Figure 7f, then constricting the production of ROS [53]. More importantly, in alkaline environments, $SO_4^{\bullet-}$ also tends to interact with OH^- (as the following equation) to afford $^\bullet OH$, which exhibits smaller half-life and redox power, causing less $SO_4^{\bullet-}$ participating in BHPM elimination.

$$SO_4^{\bullet-} + OH^- \rightarrow SO_4^{2-} + {}^\bullet OH \tag{10}$$

### 3.5. Reusability of CTO for Degradation of BHPM

Figure 8a shows BHPM degradation by using CTO for five cycles, and the used CTO could activate oxone to fully degrade BHPM continuously, confirming the recyclability of CTO. The used CTO was examined for its crystalline structure (Figure S4), which appeared similar to that of the original CTO. Additionally, its stability was also examined by analyzing whether Co was leached out. These analyses validate that CTO was a durable as well as stable activator for oxone to eliminate BHPM.

3.6. Mechanistic Insights into BHPM Elimination by CTO-Activated Oxone

Mechanistic investigation of CTO for oxone activation is also necessary. Essentially, oxone activation would afford sulfate radicals, which would evolve to other ROS. For instance, they might react with H_2O to produce $^\bullet OH$ radicals through the reaction of $SO_4^{\bullet-} + H_2O \rightarrow SO_4^{2-} + {}^\bullet OH + H^+$ [54]. Thus, $^\bullet OH$ might also participate in BHPM elimination. Several other ROS, namely superoxide ($^\bullet O_2^-$) and singlet oxygen ($^1O_2$), might also exist for degrading organic contaminants [55–57]. Therefore, it would be critical to probe into elimination mechanism of BHPM using CTO-activated oxone. To do so, the influence of radical inhibitors to BHPM degradation were scrutinized by multiple indicators, including *tert*-butyl alcohol (TBA), methanol, benzoquinone, as well as NaN_3, to identify their inhibitory influence on $^\bullet OH$, $SO_4^{\bullet-}$, $^\bullet O_2^-$, and $^1O_2$, respectively.

Initially, as TBA was firstly employed, BHPM elimination was marginally affected because k dropped to 0.204 min^{-1} (Figure 8b), indicating that $^\bullet OH$ might be present and contributing to BHPM elimination. Nevertheless, the hydroxyl radical was not reckoned as the primary ROS responsible for BHPM degradation. Additionally, when methanol was then used, BHPM elimination was significantly suppressed ($k = 0.006$ min^{-1}) (Figure 8c), suggesting that sulfate radicals were present and primarily responsible for BHPM elimination. Subsequently, as benzoquinone (BQ) and sodium azide (NaN_3) were then added and tested for their inhibitory effects, BHPM elimination was also noticeably affected, and the resulting k dropped to 0.101 and 0.011 min^{-1}. These results also demonstrate that $^\bullet O_2^-$ as well as $^1O_2$ might also be present and formed from CTO-activated oxone during BHPM degradation.

For further clarifying ROS from CTO-activated oxone, EPR tests were also conducted in Figure 8d–f. Initially, the first spin-trapping agent, 5,5-Dimethyl-1-Pyrroline-N-Oxide (DMPO), was adopted, and no distinct pattern was noted as oxone alone. However, when oxone as well as CTO were simultaneously added, a distinct signal was then found corresponding to DMPO-SO_4 and DMPO-OH.
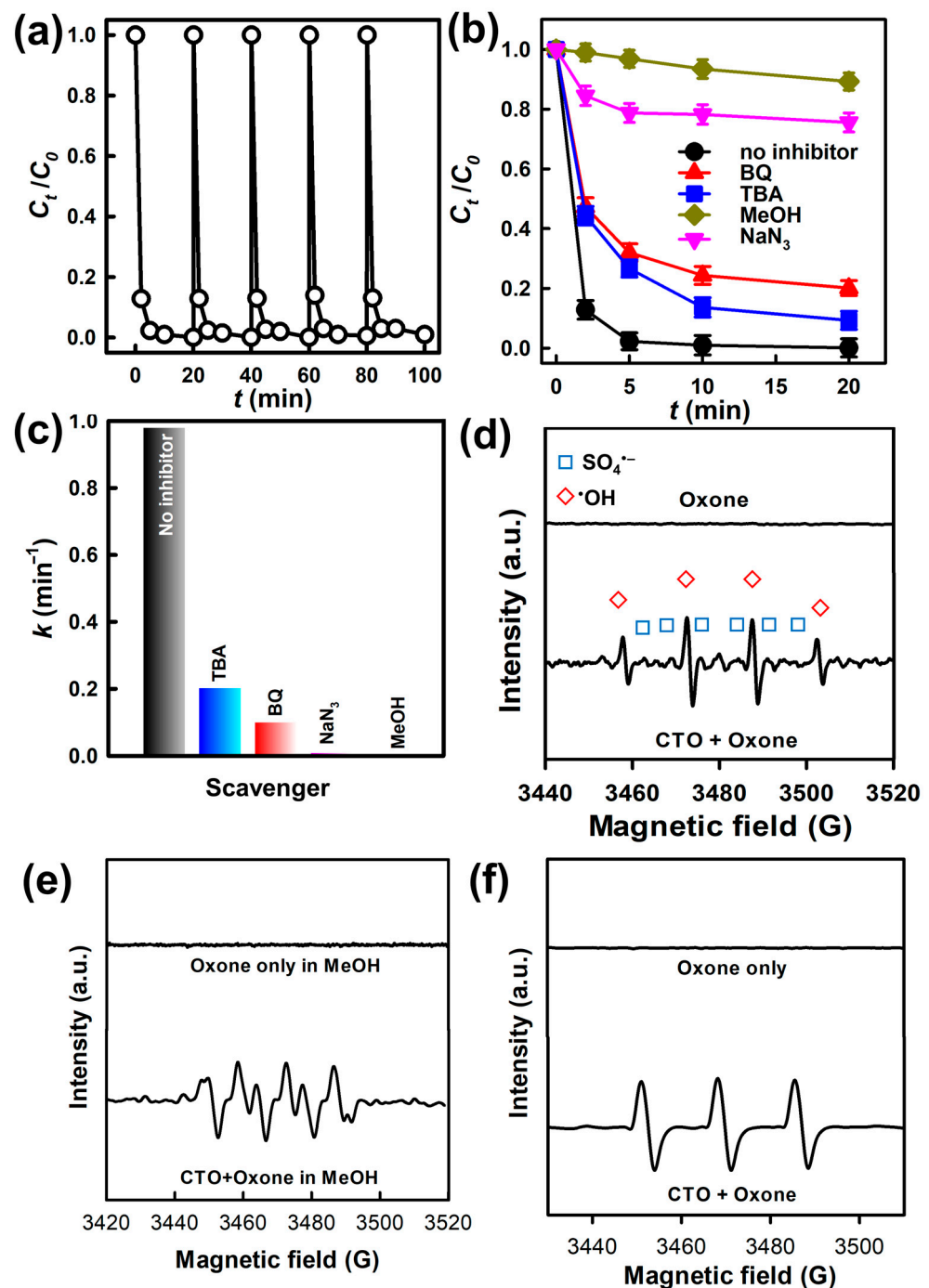
Figure 8. (**a**) Recyclability of CTO, (**b**) effect of inhibitors on BHPM degradation, and (**c**) the corresponding rate constants. EPR analyses of (**d**) DMPO-OH, DMPO-SO4, (**e**) superoxide, and (**f**) singlet oxygen (catalyst = 200 mg/L; oxone = 200 mg/L; T = 300 K).

Moreover, when the aforementioned test was conducted in a solvent of methanol, then another sextet pattern was then detected in Figure 8e corresponding to the existence of $^{\bullet}O_2^{-}$ [58]. Furthermore, when another spin-trapping agent, 2,2,6,6-Tetramethylpiperidine (TEMP), was adopted, another noticeable signal of the triplet signal was noted (Figure 8f) corresponding to the formation of 2,2,6,6-Tetramethylpiperidinyloxy (TEMPO), which was derived from the existence of singlet oxygen [59]. These analyses demonstrated that BHPM elimination by CTO-activated oxone could be ascribed to multiple ROS, namely sulfate, hydroxyl, and superoxide radicals, as well as singlet oxygen, as depicted in Figure 9.
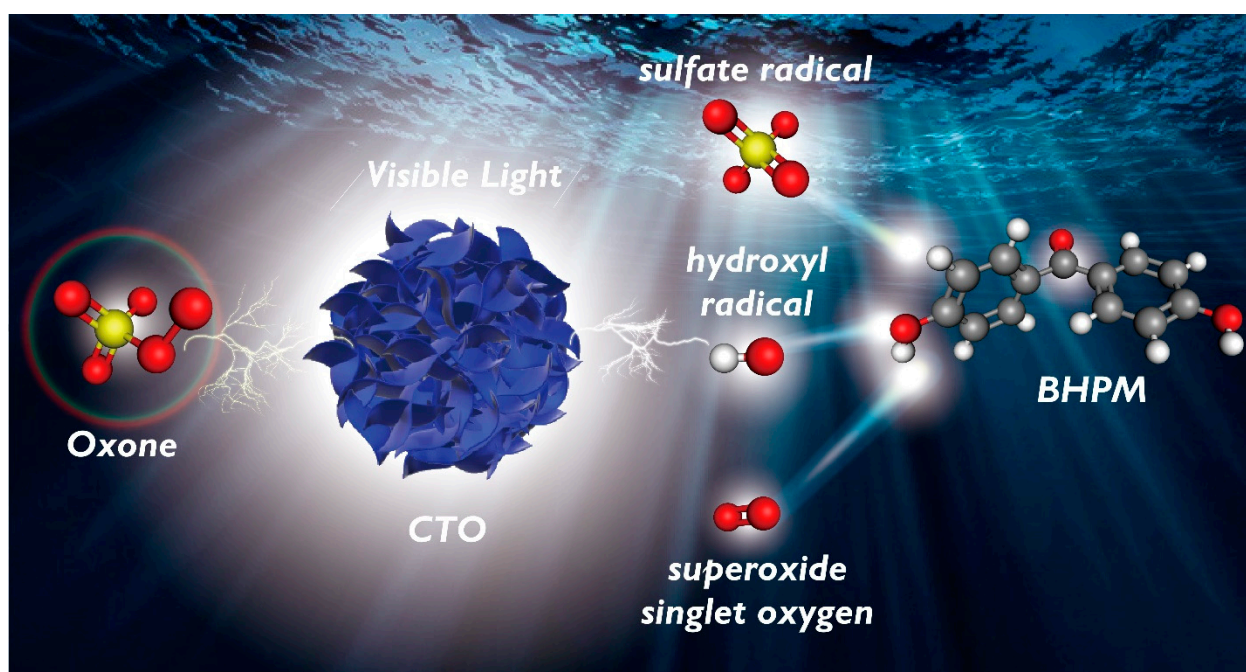
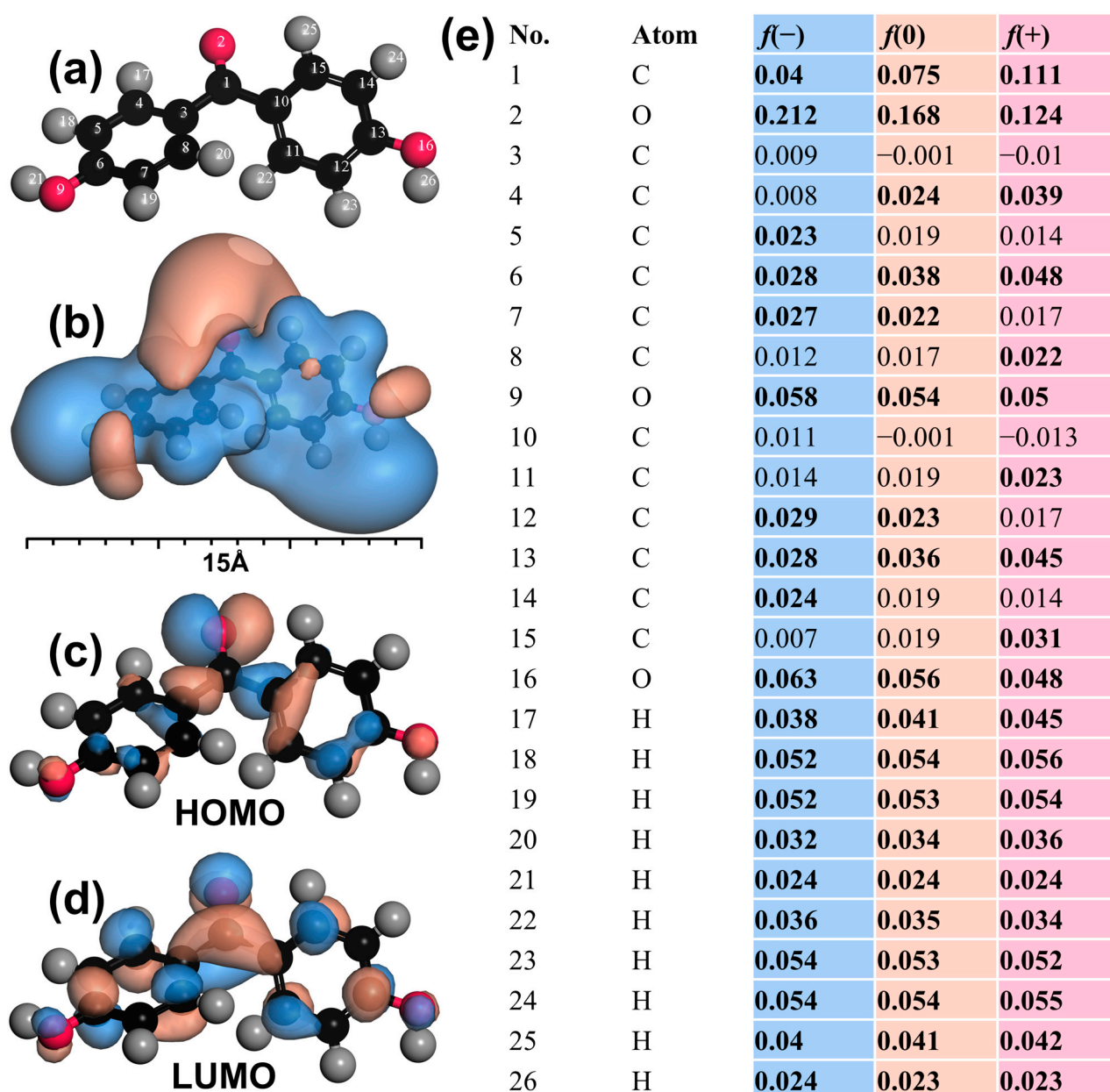**Figure 9.** The mechanistic scheme of BHPM degradation by CTO-activated oxone.

3.7. Possible BHPM Degradation Pathways and Computational Calculation

The degradation behavior of BHPM is dominated by its active sites on the structure due to the susceptibility of these sites, which can be indicated by high Fukui indexes (f^-, f^0, f^+) obtained from DFT calculation in Figure 10.

As can be seen from the BHPM structure in Figure 10a, a total of 26 atoms distributed at different sites are well-labeled, with cardinal numbers from 1 to 26 corresponding to different atoms. The ESP-mapped surface in Figure 10b highlights two distinct zones characteristic of electron-poor and electron-rich sites showed by light blue and maroon, respectively. Thus, three hydroxyl groups are regarded as most vulnerable.

For further investigating nucleophiles and electrophiles of BHPM, HOMO and LUMO are used as illustrated in Figure 10c,d. HOMO in Figure 10c shows the electron-enriched nucleophiles mapped by maroon, whereas LUMO in Figure 10d exhibits the electrophiles with insufficiency of electrons at atoms mapped by cyan, both of which are indexed by f^+ and f^- in Figure 10e. From these values, C1, O2, C4, C6, C7, O9, C12, C13, and O16 are readily able to be removed under attacks from ROS to form smaller molecules due to the high f^0 at these atoms. Meanwhile, high f^- at C1, O2, C5, C6, C7, O9, C12, C13, C14, and O16 allows these atoms to combine with their counterparts at those with high f^+, such as C1, O2, C4, C6, C8, O9, C11, C13, C15, and O16 and the nucleophile OH$^-$ in the aqueous solution.

Based on the LCQ-LC/MS spectra of BHPM degradation intermediates (Figure S5) and the above DFT calculation, there are eight degradation pathways of BHPM in total: (I) hydroxylation at O2, C5, C7, C12, and C14 with high f^-; (II) hydroxylation at O2 (high f^-) and de-hydroxylation at C6 and C13 (high f^0 at O9 and O16); (III) hydroxylation at O2, C12, and C14 (high f^- at O2, C12, and C14) and breaking at C4-C5 and C6-C7 (high f^0 at C4) and C11-C12 and C12-C13 (high f^0 at C12); (IV) breaking at C3-C4 and C4-C5 (high f^0 at C4, C7), C6-C7 and C7-C8 (high f^0 at C7), and C11-C12 and C12-C13 (high f^0 at C12); (V) de-hydroxylation at C6 and C13 (high f^0 at O9, O16); (VI) de-hydroxylation at C13 (high f^0 at O16) and breaking at C4-C5 and C6-C7 (high f^0 at C4, C7); (VII) hydroxylation at O2 (high f^-), de-hydroxylation at C13 (high f^0 at O16), and breaking at C4-C5 and C6-C7 (high f^0 at C4, C7) and C11-C12 and C12-C13 (high f^0 at C12); and (VIII) combination at O2 (high f^- and high f^+ at O2). These degradation pathways are schematically drawn in Figure 11, and all the intermediates are also listed in Table S2.

No.	Atom	$f(-)$	$f(0)$	$f(+)$
1	C	0.04	0.075	0.111
2	O	0.212	0.168	0.124
3	C	0.009	−0.001	−0.01
4	C	0.008	0.024	0.039
5	C	0.023	0.019	0.014
6	C	0.028	0.038	0.048
7	C	0.027	0.022	0.017
8	C	0.012	0.017	0.022
9	O	0.058	0.054	0.05
10	C	0.011	−0.001	−0.013
11	C	0.014	0.019	0.023
12	C	0.029	0.023	0.017
13	C	0.028	0.036	0.045
14	C	0.024	0.019	0.014
15	C	0.007	0.019	0.031
16	O	0.063	0.056	0.048
17	H	0.038	0.041	0.045
18	H	0.052	0.054	0.056
19	H	0.052	0.053	0.054
20	H	0.032	0.034	0.036
21	H	0.024	0.024	0.024
22	H	0.036	0.035	0.034
23	H	0.054	0.053	0.052
24	H	0.054	0.054	0.055
25	H	0.04	0.041	0.042
26	H	0.024	0.023	0.023

Figure 10. DFT calculation for BHPM: (**a**) the optimized molecule structure; (**b**) electrostatic potential (ESP); (**c**) the highest occupied molecular orbital (HOMO); (**d**) the lowest unoccupied molecular orbital (LUMO); and (**e**) condensed Fukui index distribution for electrophilic attack (f^-), radical attack (f^0), and nucleophilic attack (f^+).

In pathway I, the deficiency of electrons at C5, C7, C12, and C13 allowed these atoms to combine with OH^-, leading to the formation of six main intermediates from D2 to D7 (at C5, C7 for D2; at C12, C13 for D3; at C5, C13 for D4; at C7, C12 for D5; at C5, C12 for D6; and at C7, C13 for D7). From D2 in Figure S7, nine smaller molecules (D8, D21, D48, D82, D89, D116, D117, D124, and D125) were formed due to the atom detachment at C13 (for D8, high f^0 at C13); breaking at C10-C11 and C13-C14 (for D21, high f^0 at C10 and C14); breaking at C10-C11 and C13-C14 and de-hydroxylation at C4 and C6 (for D48, high f^0 at O8, C10, C14, and O16); breaking at C10-C11 and C13-C14, de-hydroxylation at C4 and C6, and atom removal at C5 (for D82, high f^0 at C5, O8, C10, C14, and O16); breaking at C10-C11 and C13-C14 and de-hydroxylation at C4, C6, and O18 and atom removal at C5 (for D89, high f^0 at C5, O8, C10, C14, O16, and O18); atom removal at C4, C6, C10, and C13 and de-hydroxylation at O18 (for D116, high f^0 at C4, C6, C10, C13, and O19); atom

removal at C4, C7, C11, and C13 and de-hydroxylation at O18 (for D117, high f^0 at C4, C7, C11, C13, and O19); atom removal at C3, C6, C11, and C13 and de-hydroxylation at O18 (for D124, high f^0 at C3, C6, C11, C13, and O19); and atom removal at C4, C6, C11, and C14 and de-hydroxylation at O18 (for D125, high f^0 at C4, C6, C11, C14, and O19). For D3 (Figure S8), similar transformation behaviors, including de-hydroxylation, breaking, and C chain fracture, were also observed, which caused the formation of D9, D10, D22, D49, D83, D90, D116, and D124. Under further attacks from ROS, these molecules continued to degrade and mineralized into CO_2 and H_2O. Meanwhile, D4 underwent the transformation through concurrent de-hydroxylation at C6, C12, and O18 (high f^0 at O15, O17, and O19) and atom removal at O18 and O19 with high f^0 to form corresponding different smaller molecules (D13, D29, and D30; see Figure S9). After formation from de-hydroxylation at C6, C12, and O18 on the structure of D4, the transformation of D13 relied on the behavior of D34 after being de-hydroxylated at C13 (high f^0 at O20, Figure S15). The D34 later went into de-hydroxylation at C12 (high f^0 at O15, Figure S34) to form D46 (one of the main intermediates in pathway V). D30 also degraded because of the same reason as that for D34, which led to the appearance of D46 as abovementioned. D29, on the other hand, transformed into different smaller molecules before terminating at D69 although D69 could also be formed directly from D29 after de-hydroxylation at C5 and C12 (high f^0 at O18 and O22) and C chain breakdown at C10-C11 and C11-C12 (high f^0 at C11) (Figure S28). During this transformation, D58 and D68 were generated owing to de-hydroxylation at C5 and C12 (for D58, high f^0 at O18 and O22), de-hydroxylation at C5 and C12m and C atom detachment at C4 with high f^0 for D68. Besides forming from D29, D68 also appeared after C atom removal at C12 (with high f^0) on the D58 structure (Figure S42). With high f^0 at O8, O15, O16, O17, and O19, D5 was easily able to be de-hydroxylated at C4, C5, C11, and O18 to become D31 and at C4, C5, and C11 (Figure S10) to become D11 in pathway II. In addition, high f^0 at C4 and C12 also made C atom at these sites to detach, forming D23. Quite similar to D23, D45 was also found to be formed after the O18-O19 bond was fractured further from D5. However, D50 was formed under the same attacks as those for D23, but two more hydroxyl groups at C5 and C13 on the structure of D5 were removed. D68 and D69 from D4 along with D23, D45, and D50 from D5 later went into mineralization to CO_2 and H_2O. Conversely, D31 from D5 was continued to be de-hydroxylated at C6 (high f^0 at O9, Figure S30) before ending at D46 in pathway V, the same as D30 and D34. Apart from transforming into D27 in pathway II due to simultaneous de-hydroxylation at C5, C6, C12, and C13 into D12 due to de-hydroxylation at C6, C12, and C13 and into D46 due to de-hydroxylation at C5, C6, C12, C13, and O18 (high f^0 at O8, O15, O16, O17, and O19, Figure S11), D6 also degraded into other molecules under the same behavior, but less hydroxyl groups and one or two more O atoms of O18 and O19 detached one OH^- at C13 and two O atoms at C1 for D14, two OH^- at C12 and C13 and one OH^- at O18 for D15, two OH^- at C12 and C13 and two O atoms at C1 for D32, three OH^- at C6, C12 and C13 and one OH^- at O18 for D34 (due to high f^0 at these atoms). After formation, D14 and D32 followed the degradation pathway of D58, while D15 followed that of D34. Finally, the last initiator of the pathway I (i.e., D7) took part in variety of transformations, such as de-hydroxylation at C4, C5, and C12 for D16; at C5, C12, and O18 for D17; at C4, C5, C11, and C12 for D27 in pathway II; at C4, C5, C12, and O18 for D33; at C4, C5, C11, C12, and O18 for D46; at C4, C5, C11, C12, and O atom removal at C1 for D58 (Figure S12). In contrast, OH^- detachment at C5 and C1-O18 cleavage accounted for the presence of D18. D35, on the other hand, was formed due to one more OH at C12 being detached besides those transformations for the appearance of D18. Similar to D15 from D6, the degradation of D17 and D33 also agreed with that of D34, while D18 and D35 degraded the same as D58 did. D16, on the contrary, became D27 after de-hydroxylation at C6 (high f^0 at O18, Figure S18).
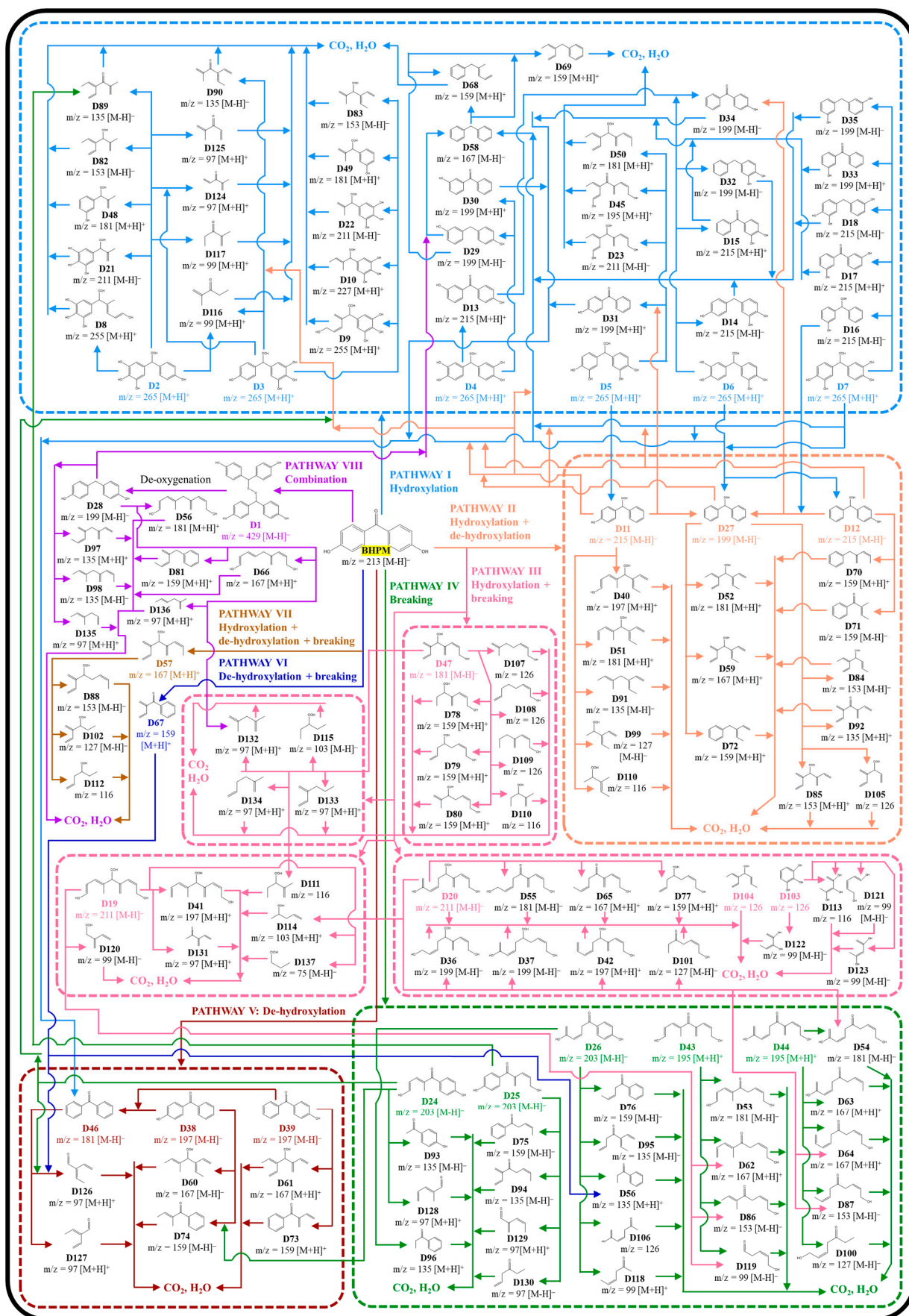
Figure 11. A proposed degradation pathway of BHPM by CTO-activated oxone.

In pathway II, both hydroxylation and de-hydroxylation dominated the transformation of BHPM, which directly allowed D11, D12, and D27 to be formed. All the reactions occurring for the presence of these molecules were mainly because of hydroxylation at C1 and de-hydroxylation at C13 for D11, hydroxylation at C1 and de-hydroxylation at C6 for D12, hydroxylation at C1, and de-hydroxylation at both C6 and C13 for D27. Later transformations of D11 were associated with the existence of D40, D51, D91, D99, and D110, which stemmed from breakdown at C5-C6 and C6-C7 and C10-C11 and C11-C12 (high f^0 at C6, C11) for D40; breakdown at C5-C6 and C6-C7 (high f^0 at C6), C10-C11 and C11-C12 (high f^0 at C11), and de-hydroxylation at C5 (high f^0 at O14) for D51; breakdown at C4-C5 and C6-C7 (high f^0 at C5 and C6) and C10-C11 and C11-C12 (high f^0 at C11) for D91; breakdown at C2-C3 and C2-C7 (high f^0 at C2 and C3) and C10-C11 and C11-C12 (high f^0 at C11) for D99; breakdown at C2-C3 and C2-C7 (high f^0 at C2 and C3) and C10-C11 and C12-C13 (high f^0 at C11 and C12) for D116 (see Figure S13). These compounds then degraded further and turned into CO_2 and H_2O as the final products. Moreover, the transformation of D11 was also involved in the formation of D27, D31, and D46 as a result of de-hydroxylation at C5 (for D27), at O15 (for D31), and at both C5 and O15 for D46. For D12, the O atom removal at C1; C atom removal at C10, C11, and C12; and de-hydroxylation at C11 and O15 were found to be the main reasons for its changes in the structure, forming D27, D46, D70, and D71 (Figure S14). Similarly, D27 was also broken down at the sites with high f^0 (C3, C5, C6, C11, C12, O14, and O15 in Figure S26) to form D46, D52, D59, D72, D84, D85, D92, and D105. These products (except for D46) would be subsequently mineralized into CO_2 and H_2O to complete the degradation of D27 in this pathway.

The next pathway contributing to the BHPM degradation was concurrent occurrence of hydroxylation and breaking initiated by the presence of five primary intermediates, including D19, D20, D47, D103, and D104. Being produced from hydroxylation and breakdown of BHPM at O and C, respectively, D47 made further degradation of BHPM more complete by participating in various reactions, dominated mainly by de-hydroxylation and C chain cleavage. The later by-products related to the transformation of D47 included D78, D79, D80, D107, D108, D109, D110, D111, D115, D132, D133, and D134. Among these, D78, D79, D80, D110, D111, and D115 were formed by C chain cleavage, while the others were formed by de-hydroxylation and cleavage at the same time. The formation of these by-products was due to the existence of active sites on the D47 structure, as shown by those with high f^0 at C4, C5, C8, C10, and O11-13 in Figure S40. After that, they continued to be destructed until the evolution of CO_2 and H_2O as the final products of D47 transformation. Similarly, D19 also behaved in the ways as those D47 did, which were directed predominantly by de-hydroxylation and breakdown, resulting in the formation of D41, D62, D86, D114, D119, D120, D131, and D137. D19 was no exception: high f^0 at C1, O2, C4, C6, C10, C12, C14, O15, and O16 on its structure (Figure S21) left it most vulnerable, thereby being destroyed into different above smaller molecules. These molecules were continually broken down so that CO_2 and H_2O appeared at the end. Having high f^0 at different sites on the structure (Figure S22), D20 followed the degradation pathways that were triggered primarily by de-hydroxylation and breakdown, leading to the presence of D36, D37, D42, D54, D55, D64, D65, D77, D87, D101, and D114. While the presence of D42 was due to de-hydroxylation at C5, breakdown was the main cause for the formation of D36, D37, D77, and D114. In contrast, D54, D55, D64, D65, D87, and D101 were formed because of the simultaneous occurrence of both de-hydroxylation and breakdown. After all, the above changes worked together, causing D20 to degrade more completely so as to leave CO_2 and H_2O at the end. For D103, de-hydroxylation at C4 and C5 and benzene ring opening obtained from C atom removal at C1 and C4 (Figure S44) were responsible for its destruction, resulting in the existence of D113 (ring opening at C1), D121 (ring opening at C4), D122 (ring opening at C1 and de-hydroxylation at C5), and D123 (ring opening at C1 and de-hydroxylation at C4). These products along with D104, another first intermediate of BHPM in this pathway, were finally mineralized into CO_2 and H_2O.

The fourth pathway was started by the participation of five major intermediates, including D24, D25, D26, D43, and D44 as a result of fracturing BHPM at C7 (for D24), C12 (for D25), C4 (for D26), C7 and C12 (for D43), and C4 and C12 (for D44). The transformation of D24 into D74, D90, D93, D96, D126, and D128, which resulted from the detachment of OH^- and C chain cleavage at the sites with high f^0 (Figure S23), brought about complete degradation of BHPM by the presence of CO_2 and H_2O afterwards. Transforming into by-products with a total quantity of one less than D24, D25 underwent the pathways so that D75, D89, D94, D129, and D130 appeared subsequently, caused by breakdown, de-hydroxylation, and C atom removal at vulnerable sites with high f^0 in Figure S24 (de-hydroxylation at C9 and C13 and C atom removal at C10 for D75; C atom removal at C8 and C13 for D89; breakdown at C2-C12 bond, de-hydroxylation at C9, and C atom removal at C10 and C13 for D94; breakdown at C1-C3 bond and de-hydroxylation at C9 for D129; and C atom removal at C5, C8, C10, and C13 for D130). Five above by-products continued to be destroyed until CO_2 and H_2O as the final products of D25 were reached. Aside from forming by C atom removal at C5 and de-hydroxylation at C9 of D24, D96 was also found to be formed from D26 as a result of breakdown at C4-C15 bond and de-hydroxylation at C8 (high f^0 at C4 and O11, Figure S25). In addition, the presence of other smaller products, such as D56, D76, D95, D106, and D118, also contributed to the D26 degradation through bond cleavage and removal of C and OH^-. While C and OH removal at C8, C12, and C13 was for D76, C removal at C8 and C13 was for D95. D56, on the other hand, was formed by C4-C15 cleavage and OH^- removal at C8. Same as D95, D106 was also formed by C removal but at C6 and C10. Through the same way leading to the formation of D106, D118 appeared after additional C removal at C12 and de-hydroxylation at C13. All these molecules were then further degraded and mineralized into CO_2 and H_2O, which were also the final products of degrading D43 and D44 but through different ways. These ways were initiated by the presence of D53, D62, D86, D119 for D43 and D54, D63, D64, D87, and D100 for D44. The reasons for the degradation of the above two primary intermediates (i.e., D43 and D44) could be explained by the availability of active sites on the corresponding structure (Figures S37 and S38), which caused two possible changes in the structure, including C atom removal and de-hydroxylation, to appear. Compared to D53, D86, D119 (in case of D43) and D54, and D100 (in case of D44), which were formed because of only C atom removal (at C13 for D53; C5 and C13 for D86; C3 and C13 for D119; C13 for D54; C7, C11, and C13 for D100), the formation of D62, D63, D64, and D87 was the result of combining both C atom removal and de-hydroxylation (C atom removal at C13 and de-hydroxylation at C5 for D62; C atom removal at C13 and de-hydroxylation at C12 for D63; C atom removal at C13 and de-hydroxylation at C6 for D64; C atom removal at C13 and C7 and de-hydroxylation at C6 for D87). Ultimately, the evolution of CO_2 and H_2O would then occur to terminate the next degradation of these smaller molecules.

The next pathway of degrading BHPM would be de-hydroxylation, which was directly related to D38, D39, and D46. As against D38 and D39, which were formed due to de-hydroxylation at either C13 (for D38) or C6 (for D39), the presence of D46 came from de-hydroxylation at both C6 and C13. Before being mineralized into CO_2 and H_2O, the above three intermediates were subjected to various transformations, which involved the formation of D46, D60, and D74 for D38; D46, D61, and D73 for D39; and D126 and D127 for D46. The remaining OH^- on the structure possessed a high f^0 value (Figures S35 and S36) that allowed D38 or D39 to be further de-hydroxylated at C13 or C6, respectively, forming D46, which later carried the role of degrading D38 and D39 into D126 and D127 through C chain cleavage at C1-C9 (high f^0 at C1) and C atom removal at C6 (high f^0 at C6) in case of D126 and C chain cleavage at C1-C3 (high f^0 at C1) and C atom removal at C12 (high f^0 at C12) in case of D127 (Figure S39). Besides converting into D46, D38 completed its degradation by leaving the presence of D60 and D74 as a result of removing C at C6, C7, and C13 (for C60) and at C6, C7 (for D74). Meanwhile, C atom removal at C6, C11, and C12 accounted for the generation of D61 from 39. Further, D73 was also produced by the same ways as D61 but without C atom removal at C6.

Next, de-hydroxylating and breaking down at C13 (high f^0 at O16) and C4-C5 and C6-C7 (high f^0 at C4, C6, and C7), respectively, initiated the BHPM degradation in pathway VI through which D67 was formed as the primary intermediate. The transformation of D67 later depended on D56 in pathway IV and D126 in pathway V. As C1, C5, C6, and C10 had high f^0 (Figure S43), D56 was formed because of the detachment of C5 and C6 at the same time, while the disappearance of C10 as well as the fracture of C1-C3 contributed to the presence of D126.

The degradation of BHPM was further enhanced by hydroxylation at O2 (high f^-), de-hydroxylation at C13 (high f^0 at O16), and breaking at C4-C5 and C6-C7 and C11-C12 and C12-13 (high f^0 at C4, C6, C12, and C13), which simultaneously caused D57 to appear. Afterwards, D88, D102, and D112 appeared as a result of destroying D57 through removal of C10 (for D88); C8 and C10 (for D102); and C5, C8, and C10 (for D112) (due to high f^0 at C5, C8, and C10 in Figure S41). These three molecules were then destroyed and mineralized into CO_2 and H_2O to finish the BHPM degradation in pathway VII.

Finally, the combination of a nucleophile with an electrophile from the BHPM molecule at O2 through donating (for nucleophile) and accepting (for electrophile) an electron pair resulted in the formation of D1, which was then deoxygenated at C1 and C32 (high f^0 at O2 and O31, Figure S6) to form D28. From here, nine other smaller molecules, including D58 (in pathway I), D132 (in pathway III), D56, D66, D81, D97, D98, D135, and D136, were produced via de-hydroxylation at C5 and C12; C atom removal at C3, C4, C6, C10, C11, and C13; and breakdown at C4-C5 and C12-C13 (because of high f^0 at C3, C4, C6, O8, C10, C11, C13, and O15 in Figure S27). Without breakdown and C atom removal, the de-hydroxylation at both C5 and C12 gave rise to D58. In contrast, D56 needed C atom removal at C6 and C11 for it to be formed. Further removal of C10 compared to D56 resulted in the appearance of D66. For D132 and D136, C atom removal was responsible for their formation, in which the removal of C at C4, C6, C11, and C13 caused D132 to appear, while C atom removal at C4, C6, and C10 and bond cleavage at C12-C13 led to the formation of D136. D135, on the other hand, was formed from removal of C at C3, C6, and C11 and bond cleavage at C12-C13. The remaining three compounds, consisting of D81, D97, and D98, were generated by de-hydroxylation at C5 and C12 and C atom removal at C13 (for D81); de-hydroxylation at C12, C atom removal at C6 and C13, and bond breakdown at C4-C5 (for D97); and de-hydroxylation at C5, C atom removal at C6 and C11, and bond breakdown at C12-C13 (for D98). The later mineralization of these compounds into CO_2 and H_2O would complete the BHPM degradation via D1 and D28 as primary and secondary intermediate, respectively, in pathway VIII.

4. Conclusions

Herein, CTO was investigated for the first time as a chemical and photocatalytic catalyst for oxone activation to eliminate an important USF, namely BHPM, from water. Especially, a special morphology of NS-assembled configuration of CTO was designed to maximize active surfaces and sites of CTO. Thus, CTO outperformed the conventional Co_3O_4 and TiO_2 NP to activate oxone to eliminate BHPM. Moreover, the substituent of Ti enabled CTO to enhance absorption of visible light and possess a much smaller E_g. These photocatalytic properties further intensified CTO's activity for oxone activation via photocatalysis. CTO also possessed a smaller E_a of elimination of USFs than the reported catalytic systems, revealing its advantage over the existing reported catalysts. Moreover, the degradation mechanism of BHPM by CTO-activated oxone was also elucidated using the tests of scavengers and EPR for identifying the presence and contribution of ROS to BHPM degradation. The BHPM degradation mechanism was elucidated, and the degradation pathway was also investigated and unveiled in details via the DFT calculation. These results validate that CTO appeared as a superior heterogeneous catalyst for oxone activation to eliminate BHPM.

References

1. Pintado-Herrera, M.G.; Lara-Martín, P.A.; González-Mazo, E.; Allan, I.J. Determination of silicone rubber and low-density polyethylene diffusion and polymer/water partition coefficients for emerging contaminants. *Environ. Toxicol. Chem.* **2016**, *35*, 2162–2172. [CrossRef] [PubMed]

2. Tsui, M.M.P.; Leung, H.W.; Wai, T.-C.; Yamashita, N.; Taniyasu, S.; Liu, W.; Lam, P.K.S.; Murphy, M.B. Occurrence, distribution and ecological risk assessment of multiple classes of UV filters in surface waters from different countries. *Water Res.* **2014**, *67*, 55–65. [CrossRef] [PubMed]

3. Parker, D.; Bussink, J.; van de Grampel, H.T.; Wheatley, G.W.; Dorf, E.-U.; Ostlinning, E.; Reinking, K. Polymers, High-Temperature. In *Ullmann's Encyclopedia of Industrial Chemistry*; Wiley-VCH: Hoboken, NJ, USA, 1914.

4. Eddine, A.N.; von Kries, J.P.; Podust, M.V.; Warrier, T.; Kaufmann, S.H.E.; Podust, L.M. X-ray Structure of 4,4′-Dihydroxybenzophenone Mimicking Sterol Substrate in the Active Site of Sterol 14α-Demethylase (CYP51)*♦. *J. Biol. Chem.* **2008**, *283*, 15152–15159. [CrossRef] [PubMed]

5. Fast, S.A.; Gude, V.G.; Truax, D.D.; Martin, J.; Magbanua, B.S. A Critical Evaluation of Advanced Oxidation Processes for Emerging Contaminants Removal. *Environ. Process.* **2017**, *4*, 283–302. [CrossRef]

6. Andrew Lin, K.-Y.; Hsu, F.-K.; Lee, W.-D. Magnetic cobalt-graphene nanocomposite derived from self-assembly of MOFs with graphene oxide as an activator for peroxymonosulfate. *J. Mater. Chem. A* **2015**, *3*, 9480–9490. [CrossRef]

7. Li, M.-C.; Ghanbari, F.; Chang, F.-C.; Hu, C.; Lin, K.-Y.A.; Du, Y. Enhanced degradation of 5-sulfosalicylic acid using peroxymonosulfate activated by ordered porous silica-confined Co_3O_4 prepared via a solvent-free confined space strategy. *Sep. Purif. Technol.* **2020**, *249*, 116972. [CrossRef]

8. Trang, N.H.; Kwon, E.; Lisak, G.; Hu, C.; Andrew Lin, K.-Y. Cobalt ferrite nanoparticle-loaded nitrogen-doped carbon sponge as a magnetic 3D heterogeneous catalyst for monopersulfate-based oxidation of salicylic acid. *Chemosphere* **2021**, *267*, 128906. [CrossRef]

9. Yang, Q.; Choi, H.; Al-Abed, S.R.; Dionysiou, D.D. Iron–cobalt mixed oxide nanocatalysts: Heterogeneous peroxymonosulfate activation, cobalt leaching, and ferromagnetic properties for environmental applications. *Appl. Catal. B Environ.* **2009**, *88*, 462–469. [CrossRef]

10. Cai, C.; Zhang, H.; Zhong, X.; Hou, L. Ultrasound enhanced heterogeneous activation of peroxymonosulfate by a bimetallic Fe–Co/SBA-15 catalyst for the degradation of Orange II in water. *J. Hazard. Mater.* **2015**, *283*, 70–79. [CrossRef]

11. Anipsitakis, G.P.; Stathatos, E.; Dionysiou, D.D. Heterogeneous Activation of Oxone Using Co_3O_4. *J. Phys. Chem. B* **2005**, *109*, 13052–13055. [CrossRef]

12. Tuan, D.D.; Hu, C.; Kwon, E.; Du, Y.; Lin, K.-Y.A. Coordination polymer-derived porous Co_3O_4 nanosheet as an effective catalyst for activating peroxymonosulfate to degrade sulfosalicylic acid. *Appl. Surf. Sci.* **2020**, *532*, 147382. [CrossRef]

13. Chen, X.; van Gog, H.; van Huis, M.A. Transformation of Co_3O_4 nanoparticles to CoO monitored by in situ TEM and predicted ferromagnetism at the Co_3O_4/CoO interface from first principles. *J. Mater. Chem. C* **2021**, *9*, 5662–5675. [CrossRef]

14. Chen, X.; Chen, J.; Qiao, X.; Wang, D.; Cai, X. Performance of nano-Co_3O_4/peroxymonosulfate system: Kinetics and mechanism study using Acid Orange 7 as a model compound. *Appl. Catal. B* **2008**, *80*, 116–121. [CrossRef]

15. Guan, Z.-Y.; Kwon, E.; Lee, J.; Lin, Y.-F.; Lin, K.-Y.A. Electrospun cobalt ferrite nanofiber as a magnetic and effective heterogeneous catalyst for activating peroxymonosulfate to degrade sulfosalicylic acid. *Sep. Purif. Technol.* **2021**, *259*, 118163. [CrossRef]

16. Yun, W.-C.; Lin, K.-Y.A.; Tong, W.-C.; Lin, Y.-F.; Du, Y. Enhanced degradation of paracetamol in water using sulfate radical-based advanced oxidation processes catalyzed by 3-dimensional Co_3O_4 nanoflower. *Chem. Eng. J.* **2019**, *373*, 1329–1337. [CrossRef]

17. Sun, H.; Ullah, R.; Chong, S.; Ang, H.M.; Tadé, M.O.; Wang, S. Room-light-induced indoor air purification using an efficient Pt/N-TiO_2 photocatalyst. *Appl. Catal. B* **2011**, *108*, 127–133. [CrossRef]

18. Matalkeh, M.; Nasrallah, G.K.; Shurrab, F.M.; Al-Absi, E.S.; Mohammed, W.; Elzatahry, A.; Saoud, K.M. Visible Light Photocatalytic Activity of Ag/WO$_3$ Nanoparticles and its Antibacterial Activity Under Ambient Light and in The Dark. *Results Eng.* **2022**, *13*, 100313. [CrossRef]

19. Rahimi-Nasrabadi, M.; Ghaderi, A.; Banafshe, H.R.; Eghbali-Arani, M.; Akbari, M.; Ahmadi, F.; Pourmasoud, S.; Sobhani-Nasab, A. Preparation of Co$_2$TiO$_4$/CoTiO$_3$/Polyaniline ternary nano-hybrids for enhanced destruction of agriculture poison and organic dyes under visible-light irradiation. *J. Mater. Sci. Mater. Electron.* **2019**, *30*, 15854–15868. [CrossRef]

20. Ramezani, M.; Hosseinpour-Mashkani, S.M. Controlled Synthesis, Characterization, and Photocatalytic Application of Co$_2$TiO$_4$ Nanoparticles. *J. Electron. Mater.* **2017**, *46*, 1371–1377. [CrossRef]

21. Zhang, L.; Yu, J.C.; Yip, H.Y.; Li, Q.; Kwong, K.W.; Xu, A.-W.; Wong, P.K. Ambient Light Reduction Strategy to Synthesize Silver Nanoparticles and Silver-Coated TiO$_2$ with Enhanced Photocatalytic and Bactericidal Activities. *Langmuir* **2003**, *19*, 10372–10380. [CrossRef]

22. Andrew Lin, K.-Y.; Zhang, Z.-Y. α-Sulfur as a metal-free catalyst to activate peroxymonosulfate under visible light irradiation for decolorization. *RSC Adv.* **2016**, *6*, 15027–15034. [CrossRef]

23. Lin, K.-Y.A.; Zhang, Z.-Y. Metal-free activation of Oxone using one-step prepared sulfur-doped carbon nitride under visible light irradiation. *Sep. Purif. Technol.* **2017**, *173*, 72–79. [CrossRef]

24. Zhang, M.-W.; Lin, K.-Y.A.; Huang, C.-F.; Tong, S. Enhanced degradation of toxic azo dye, amaranth, in water using Oxone catalyzed by MIL-101-NH2 under visible light irradiation. *Sep. Purif. Technol.* **2019**, *227*, 115632. [CrossRef]

25. Guo, X.; Liang, J.; Wang, L.; Feng, Z.; Yu, T.; Zhang, Z.; Shao, Y.; Hao, C.; Li, G. Synthesis of Cobalt–Glycerate hierarchical structure and their conversion into hierarchical CoP nanospheres for the hydrogen evolution reaction. *Int. J. Hydrogen Energy* **2018**, *43*, 2034–2042. [CrossRef]

26. Yang, Z.K.; Song, L.X.; Teng, Y.; Xia, J. Ethylenediamine-modulated synthesis of highly monodisperse copper sulfide microflowers with excellent photocatalytic performance. *J. Mater. Chem. A* **2014**, *2*, 20004–20009. [CrossRef]

27. Lai, H.-K.; Chou, Y.-Z.; Lee, M.-H.; Lin, K.-Y.A. Coordination polymer-derived cobalt nanoparticle-embedded carbon nanocomposite as a magnetic multi-functional catalyst for energy generation and biomass conversion. *Chem. Eng. J.* **2018**, *332*, 717–726. [CrossRef]

28. Lin, K.-Y.A.; Chang, H.-A.; Chen, R.-C. MOF-derived magnetic carbonaceous nanocomposite as a heterogeneous catalyst to activate oxone for decolorization of Rhodamine B in water. *Chemosphere* **2015**, *130*, 66–72. [CrossRef]

29. Khiem, T.C.; Tuan, D.D.; Kwon, E.; Thanh, B.X.; Tsang, Y.F.; Munagapati, V.S.; Wen, J.-C.; Hu, C.; Lin, K.-Y. Hollow and Oval-Configured Ultrafine Co$_3$O$_4$ as a Highly-Efficient Activator of Monopersulfate for Catalytic Elimination of Azorubin S. *Sustain. Environ. Res.* **2022**. [CrossRef]

30. Liu, W.-J.; Kwon, E.; Huy, N.N.; Khiem, T.C.; Lisak, G.; Wi-Afedzi, T.; Wu, C.-C.; Ghanbari, F.; Lin, K.-Y.A. Facilely-prepared sulfide-doped Co$_3$O$_4$ nanocomposite as a boosted catalyst for activating Oxone to degrade a sunscreen agent. *J. Taiwan Inst. Chem. Eng.* **2022**, *133*, 104253. [CrossRef]

31. Shafiee, M.R.M.; Parhizkar, J.; Radfar, S. Removal of Rhodamine B by g-C$_3$N$_4$/Co$_3$O$_4$/MWCNT composite stabilized in hydrogel via the synergy of adsorption and photocatalysis under visible light. *J. Mater. Sci. Mater. Electron.* **2019**, *30*, 12475–12486. [CrossRef]

32. Tai, J.Y.; Leong, K.H.; Saravanan, P.; Aziz, A.A.; Sim, L.C. Dopant-free oxygen-rich titanium dioxide: LED light-induced photocatalysis and mechanism insight. *J. Mater. Sci.* **2017**, *52*, 11630–11642. [CrossRef]

33. Kaewkam, P.; Kanchanapaetnukul, A.; Khamyan, J.; Phadmanee, N.; Lin, K.-Y.A.; Kobwittaya, K.; Sirivithayapakorn, S. UV-assisted TiO2 photocatalytic degradation of virgin LDPE films: Effect of UV-A, UV-C, and TiO$_2$. *J. Environ. Chem. Eng.* **2022**, *10*, 108131. [CrossRef]

34. Ningsih, L.A.; Yoshida, M.; Sakai, A.; Lin, K.-Y.A.; Wu, K.C.; Catherine, H.N.; Ahamad, T.; Hu, C. Ag-modified TiO2/SiO2/Fe3O4 sphere with core-shell structure for photo-assisted reduction of 4-nitrophenol. *Environ. Res.* **2022**, *214*, 113690. [CrossRef]

35. Khanahmadzadeh, S.; Enhessari, M.; Solati, Z.; Mohebalizadeh, A.; Alipouramjad, A. Synthesis, characterization and optical band gap of the Co$_2$TiO$_4$ nanoparticles. *Mater. Sci. Semicond. Process.* **2015**, *31*, 599–603. [CrossRef]

36. Jiang, Z.; Lu, W.; Li, Z.; HO, K.H.; Li, X.; Jiao, X.; Chen, D. Synthesis of amorphous cobalt sulfide polyhedral nanocages for high performance supercapacitors. *J. Mater. Chem. A* **2014**, *2*, 8603–8606. [CrossRef]

37. Li, Y.; Li, F.-M.; Meng, X.-Y.; Li, S.-N.; Zeng, J.-H.; Chen, Y. Ultrathin Co$_3$O$_4$ Nanomeshes for the Oxygen Evolution Reaction. *ACS Catal.* **2018**, *8*, 1913–1920. [CrossRef]

38. Hu, P.D.; Long, M.C. Cobalt-catalyzed sulfate radical-based advanced oxidation: A review on heterogeneous catalysts and applications. *Appl. Catal. B-Environ.* **2016**, *181*, 103–117. [CrossRef]

39. Thota, S.; Reehuis, M.; Maljuk, A.; Hoser, A.; Hoffmann, J.U.; Weise, B.; Waske, A.; Krautz, M.; Joshi, D.; Nayak, S.; et al. Neutron diffraction study of the inverse spinels Co$_2$TiO$_4$ and Co$_2$SnO$_4$. *Phys. Rev. B* **2017**, *96*, 144104. [CrossRef]

40. Yan, S.C.; Li, Z.S.; Zou, Z.G. Photodegradation of Rhodamine B and Methyl Orange over Boron-Doped g-C$_3$N$_4$ under Visible Light Irradiation. *Langmuir* **2010**, *26*, 3894–3901. [CrossRef]

41. Chen, X.; Wang, W.; Xiao, H.; Hong, C.; Zhu, F.; Yao, Y.; Xue, Z. Accelerated TiO2 photocatalytic degradation of Acid Orange 7 under visible light mediated by peroxymonosulfate. *Chem. Eng. J.* **2012**, *193*, 290–295. [CrossRef]

42. Othman, I.; Hisham Zain, J.; Abu Haija, M.; Banat, F. Catalytic activation of peroxymonosulfate using CeVO$_4$ for phenol degradation: An insight into the reaction pathway. *Appl. Catal. B* **2020**, *266*, 118601. [CrossRef]

43. Tang, W.; Zhang, Y.; Guo, H.; Liu, Y. Heterogeneous activation of peroxymonosulfate for bisphenol AF degradation with BiOI$_{0.5}$Cl$_{0.5}$. *RSC Adv.* **2019**, *9*, 14060–14071. [CrossRef]

44. Guo, S.; Zhang, L.; Chen, M.; Ahmad, F.; Fida, H.; Zhang, H. Heterogeneous Activation of Peroxymonosulfate by a Spinel CoAl$_2$O$_4$ Catalyst for the Degradation of Organic Pollutants. *Catalysts* **2022**, *12*, 847. [CrossRef]

45. Liu, W.-J.; Park, Y.-K.; Chen, W.-H.; Bui, H.M.; Munagapati, V.S.; Tuan, D.D.; Wen, J.-C.; You, S.; Da Oh, W.; Lin, K.-Y.A. Highly-efficient degradation of ensulizole using monopersulfate activated by nanostructured cobalt oxide: A comparative study on effects of different nanostructures. *J. Environ. Chem. Eng.* **2022**, *10*, 107137. [CrossRef]

46. Yin, J.-Y.; Oh, W.D.; Kwon, E.; Thanh, B.X.; You, S.; Wang, H.; Lin, K.-Y.A. Cobalt sulfide nanofilm-assembled cube as an efficient catalyst for activating monopersulfate to degrade UV filter, 4,4′-dihydroxybenzophenone, in water. *Colloids Surf. A Physicochem. Eng. Asp.* **2021**, *625*, 126891. [CrossRef]

47. Lin, K.-Y.A.; Lin, J.-T.; Jochems, A.P. Oxidation of amaranth dye by persulfate and peroxymonosulfate activated by ferrocene. *J. Chem. Technol. Biotechnol.* **2017**, *92*, 163–172. [CrossRef]

48. Lin, K.-Y.A.; Lin, T.-Y. Degradation of Acid Azo Dyes Using Oxone Activated by Cobalt Titanate Perovskite. *Water Air Soil Pollut.* **2017**, *229*, 10. [CrossRef]

49. Lin, K.-Y.A.; Lin, J.-T.; Lin, Y.-F. Heterogeneous catalytic activation of percarbonate by ferrocene for degradation of toxic amaranth dye in water. *J. Taiwan Inst. Chem. Eng.* **2017**, *78*, 144–149. [CrossRef]

50. Tan, C.; Gao, N.; Deng, Y.; Deng, J.; Zhou, S.; Li, J.; Xin, X. Radical induced degradation of acetaminophen with Fe$_3$O$_4$ magnetic nanoparticles as heterogeneous activator of peroxymonosulfate. *J. Hazard. Mater.* **2014**, *276*, 452–460. [CrossRef]

51. Imamović, B.; Trebše, P.; Omeragić, E.; Bečić, E.; Pečet, A.; Dedić, M. Stability and Removal of Benzophenone-Type UV Filters from Water Matrices by Advanced Oxidation Processes. *Molecules* **2022**, *27*, 1874. [CrossRef]

52. Kang, S.; Hwang, J. CoMn$_2$O$_4$ embedded hollow activated carbon nanofibers as a novel peroxymonosulfate activator. *Chem. Eng. J.* **2021**, *406*, 127158. [CrossRef]

53. Guo, W.; Su, S.; Yi, C.; Ma, Z. Degradation of antibiotics amoxicillin by Co$_3$O$_4$-catalyzed peroxymonosulfate system. *Environ. Prog. Sustain. Energy* **2013**, *32*, 193–197. [CrossRef]

54. Xu, L.J.; Chu, W.; Gan, L. Environmental application of graphene-based CoFe$_2$O$_4$ as an activator of peroxymonosulfate for the degradation of a plasticizer. *Chem. Eng. J.* **2015**, *263*, 435–443. [CrossRef]

55. Liang, P.; Zhang, C.; Duan, X.; Sun, H.; Liu, S.; Tade, M.O.; Wang, S. An insight into metal organic framework derived N-doped graphene for the oxidative degradation of persistent contaminants: Formation mechanism and generation of singlet oxygen from peroxymonosulfate. *Environ. Sci. Nano* **2017**, *4*, 315–324. [CrossRef]

56. Luo, R.; Li, M.; Wang, C.; Zhang, M.; Nasir Khan, M.A.; Sun, X.; Shen, J.; Han, W.; Wang, L.; Li, J. Singlet oxygen-dominated non-radical oxidation process for efficient degradation of bisphenol A under high salinity condition. *Water Res.* **2019**, *148*, 416–424. [CrossRef]

57. Yang, S.; Wu, P.; Liu, J.; Chen, M.; Ahmed, Z.; Zhu, N. Efficient removal of bisphenol A by superoxide radical and singlet oxygen generated from peroxymonosulfate activated with Fe0-montmorillonite. *Chem. Eng. J.* **2018**, *350*, 484–495. [CrossRef]

58. Hailili, R.; Wang, C.; Lichtfouse, E. Perovskite nanostructures assembled in molten salt based on halogen anions KX (X = F, Cl and Br): Regulated morphology and defect-mediated photocatalytic activity. *Appl. Catal. B* **2018**, *232*, 531–543. [CrossRef]

59. Latch, D.E.; McNeill, K. Microheterogeneity of singlet oxygen distributions in irradiated humic acid solutions. *Science* **2006**, *311*, 1743–1747. [CrossRef]

60. Waclawek, S.; Grubel, K.; Cernik, M. Simple spectrophotometric determination of monopersulfate. *Spectrochim. Acta A Mol. Biomol. Spectrosc.* **2015**, *149*, 928–933. [CrossRef]

61. Tuan, D.D.; Kwon, E.; Phattarapattamawong, S.; Thanh, B.X.; Khiem, T.C.; Lisak, G.; Wang, H.; Lin, K.-Y.A. Nitrogen-containing carbon hollow nanocube-confined cobalt nanoparticle as a magnetic and efficient catalyst for activating monopersulfate to degrade a UV filter in water. *J. Environ. Chem. Eng.* **2022**, *10*, 106989. [CrossRef]

62. Ma, J.; Feng, Y.; Yang, X.; Wu, Y.; Wang, S.; Zhang, C.; Shi, Q. Sulphate radical oxidation of benzophenone: Kinetics, mechanisms and influence of water matrix anions. *Environ. Technol.* **2021**, *42*, 4324–4332. [CrossRef]